

THE STELLAR POPULATION STRUCTURE OF THE GALACTIC DISK

JO BOVY^{1,2,3}, HANS-WALTER RIX⁴, EDWARD F. SCHLAFLY⁴, DAVID L. NIDEVER⁵, JON A. HOLTZMAN⁶,
MATTHEW SHETRONE⁷, AND TIMOTHY C. BEERS⁸

ABSTRACT

The spatial structure of stellar populations with different chemical abundances in the Milky Way contains a wealth of information on Galactic evolution over cosmic time. We use data on 14,699 red-clump stars from the APOGEE survey, covering $4 \text{ kpc} \lesssim R \lesssim 15 \text{ kpc}$, to determine the structure of mono-abundance populations (MAPs)—stars in narrow bins in $[\alpha/\text{Fe}]$ and $[\text{Fe}/\text{H}]$ —accounting for the complex effects of the APOGEE selection function and the spatially-variable dust obscuration. We determine that all MAPs with enhanced $[\alpha/\text{Fe}]$ are centrally concentrated and are well-described as exponentials with a scale length of $2.2 \pm 0.2 \text{ kpc}$ over the whole radial range of the disk. We discover that the surface-density profiles of low- $[\alpha/\text{Fe}]$ MAPs are complex: they do not monotonically decrease outwards, but rather display a peak radius ranging from $\approx 5 \text{ kpc}$ to $\approx 13 \text{ kpc}$ at low $[\text{Fe}/\text{H}]$. The extensive radial coverage of the data allows us to measure radial trends in the thickness of each MAP. While high- $[\alpha/\text{Fe}]$ MAPs have constant scale heights, low- $[\alpha/\text{Fe}]$ MAPs flare. We confirm, now with high-precision abundances, previous results that each MAP contains only a single vertical scale height and that low- $[\text{Fe}/\text{H}]$, low- $[\alpha/\text{Fe}]$ and high- $[\text{Fe}/\text{H}]$, high- $[\alpha/\text{Fe}]$ MAPs have intermediate ($h_z \approx 300\text{--}600 \text{ pc}$) scale heights that smoothly bridge the traditional thin- and thick-disk divide. That the high- $[\alpha/\text{Fe}]$, thick disk components do not flare is strong evidence against their thickness being caused by radial migration. The correspondence between the radial structure and chemical-enrichment age of stellar populations is clear confirmation of the inside-out growth of galactic disks. The details of these relations will constrain the variety of physical conditions under which stars form throughout the MW disk.

Subject headings: Galaxy: abundances — Galaxy: disk — Galaxy: evolution — Galaxy: formation — Galaxy: fundamental parameters — Galaxy: structure

1. INTRODUCTION

Understanding the growth and evolution of galactic disks is a central problem in galaxy formation. Empirical studies in this area employ two complementary approaches to investigate changes in the structure of galactic disks over cosmic time. One of them, the “look-back approach”, is based on extensive samples of galaxies that span redshifts from the time at which disks form ($z \approx 2.5$) to today ($z \approx 0$), matching corresponding samples across epochs (e.g., van Dokkum et al. 2013; Wisnioski et al. 2015). Such studies have been successful in establishing the evolution of the galaxy population properties, but they are limited to characterizing individual galaxies by quantities integrated over their stellar populations, e.g., by their size, shape, or overall velocity dispersion. The second approach, Galactic archaeology, aims at obtaining detailed observations of local galaxies, either through resolving their stellar popula-

tions into individual stars (e.g., Dalcanton et al. 2012) or using integral-field spectroscopy, trying to directly reconstruct their individual formation history. The Milky Way (MW) is perhaps the best case for Galactic archaeology, because it has very typical gross properties (e.g., mass) and because we can measure the detailed properties—six-dimensional phase-space distribution, age, elemental abundances—of large numbers of stars (Rix & Bovy 2013).

The growth of the MW disk over time is encoded in the orbital distribution of stars and their ages and elemental abundances. The radial distribution of stars of different ages and abundances constrains in particular the epochs and physical conditions under which different parts of the MW formed stars. However, the large-scale radial structure of the MW disk has been difficult to determine for any well-defined stellar tracer, primarily due to severe dust extinction in the mid-plane. Investigations have therefore been limited to measurements of the overall radial profile, which can be characterized as an approximately exponential disk (e.g., Kent et al. 1991; Benjamin et al. 2005; Jurić et al. 2008; Bovy & Rix 2013). Radial population changes in the Galactic disk have traditionally been characterized by a metallicity gradient, taking at each radius the mean over the complex abundance distribution (e.g., Audouze & Tinsley 1976; Chen et al. 2003; Anders et al. 2014; Hayden et al. 2014). Neither of these measurements provides a direct empirical constraint on the growth of the MW disk over time, nor have they proven to be very constraining for simulations of the formation of galactic disks.

¹ Department of Astronomy and Astrophysics, University of Toronto, 50 St. George Street, Toronto, ON, M5S 3H4, Canada; bovy@astro.utoronto.ca

² Institute for Advanced Study, Einstein Drive, Princeton, NJ 08540, USA

³ John Bahcall Fellow

⁴ Max-Planck-Institut für Astronomie, Königstuhl 17, D-69117 Heidelberg, Germany

⁵ Department of Astronomy, University of Michigan, Ann Arbor, MI 48109, USA

⁶ New Mexico State University, Las Cruces, NM 88003, USA

⁷ The University of Texas at Austin, McDonald Observatory, TX 79734, USA

⁸ Department of Physics and JINA Center for the Evolution of the Elements, University of Notre Dame, Notre Dame, IN 46556, USA

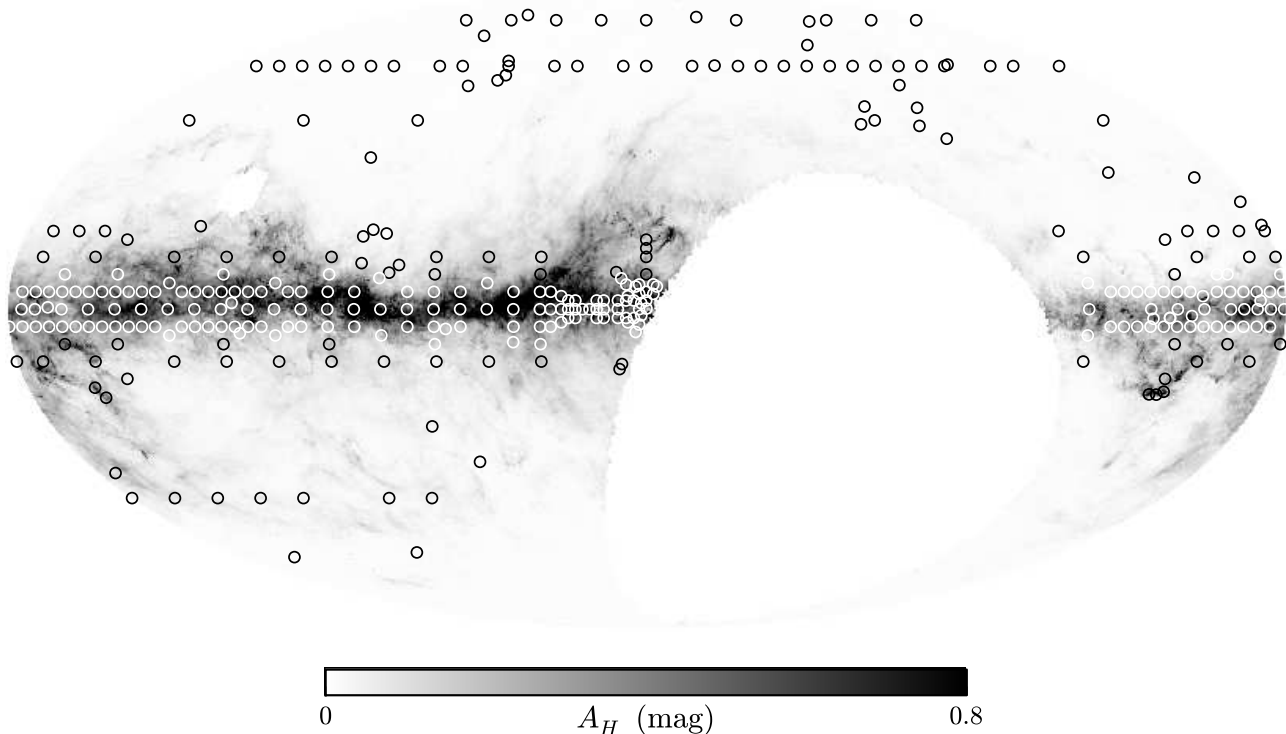


FIG. 1.— Distribution of the APOGEE fields that contain the statistical APOGEE-RC sample on the sky, overlaid on the extinction map from Green et al. (2015) at 5 kpc. Fields at $|b| < 8^\circ$ are displayed in white to enhance their contrast. The upper limit of $A_H = 0.8$ mag is the highest extinction for which the RC can be seen to 5 kpc in APOGEE medium-deep fields ($H < 12.2$). The statistical APOGEE-RC has excellent coverage of the large portion of the Galactic plane that can be seen from the Northern hemisphere (the large white region is unobserved by both APOGEE and Pan-STARRS).

Bovy et al. (2012c) suggested a different way to look at the complex correlations between spatial structure and abundances of the Galactic disk population, by separately determining disk structure of so-called mono-abundance populations (MAPs). These are subsets of stars selected to have very similar abundances, such as $[\text{Fe}/\text{H}]$ and average $[\alpha/\text{Fe}]$; for each star these abundances constitute life-long tags that remain invariant even if their orbits change grossly after birth. Beyond this simple fact, a decomposition of the disk in terms of MAPs is essentially empirical and does not assume or imply a common formation site or epoch; the detailed relation between MAPs and the underlying chemical evolution of the MW requires models and measurements of the age distributions within MAPs. Bovy et al. (2012c) were the first to attempt dissecting the radial stellar population structure of the MW disk, by measuring the radial profiles of MAPs over a few kpc near the Sun. These measurements revealed a complex abundance-dependence of the radial disk structure—both on $[\text{Fe}/\text{H}]$ and an average $[\alpha/\text{Fe}]$ —with older, $[\alpha/\text{Fe}]$ -enhanced populations having centrally-concentrated profiles and younger, solar- $[\alpha/\text{Fe}]$ populations having more extended profiles reaching the outer disk. However, the limited radial coverage and high-latitude survey geometry of the SDSS/SEGUE sample (Yanny et al. 2009) impeded more detailed measurements of the radial surface density profile beyond characterizing the local slope (in radius) by

an exponential-disk scale length.

The vertical profile of the MW, near the Sun and at other radii, is also of great interest for understanding the MW, although its interpretation in terms of stellar disk growth and evolution is still unsettled. In the solar neighborhood, the overall vertical stellar density profile (that is, of all stars) can be accurately characterized as a sum of two exponential components (Yoshii 1982; Gilmore & Reid 1983; Jurić et al. 2008; Rix & Bovy 2013), with stars in the thicker of the two components being older, more metal-poor, and $[\alpha/\text{Fe}]$ -enhanced with respect to stars in the thinner components (Fuhrmann 1998; Prochaska et al. 2000; Bensby et al. 2005; Reddy et al. 2006; Haywood et al. 2013). Dissecting the disk into MAPs, Bovy et al. (2012a,b,c) demonstrated that this broader picture is the consequence of an underlying disk structure composed of a continuum of disks, with a smooth correlation between abundance, scale height, and velocity dispersion. While the vertical profile near the Sun is composed of a smooth continuum of disk thicknesses, it has become clear from unbiased observations of element abundances of disk stars that their distribution in ($[\text{Fe}/\text{H}]$, $[\alpha/\text{Fe}]$) is distinctly bimodal, composed of two sequences—high- and low- $[\alpha/\text{Fe}]$ —that are disjoint at low- $[\text{Fe}/\text{H}]$ and that merge near solar $[\text{Fe}/\text{H}]$ (Adibekyan et al. 2012; Nidever et al. 2014). The high- $[\alpha/\text{Fe}]$ sequence becomes more prominent in the inner Galaxy, while the low- $[\alpha/\text{Fe}]$ and in par-

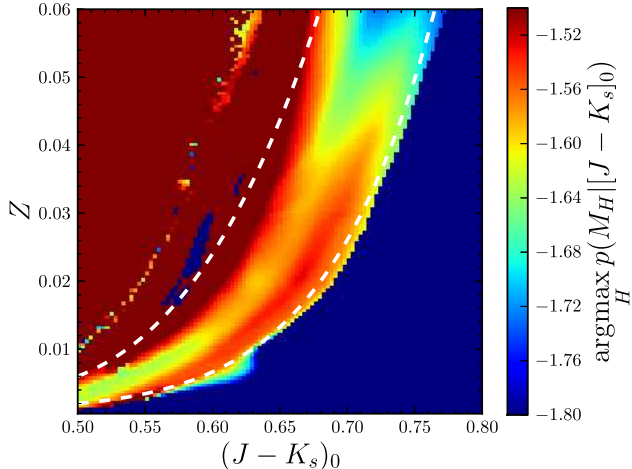


FIG. 2.— Peak of the absolute-magnitude PDF $p(M_H | [(J - K_s)_0, Z])$ as a function of color $(J - K_s)_0$ and metallicity Z for PARSEC isochrones in the RC-star region (defined using Equations [2] and [3] of Bovy et al. 2014). The white dashed lines represent the region specified by the cuts in Equations (6) and (7) of Bovy et al. (2014) that delineate the regions over which the distribution of absolute K_s magnitudes is narrow; these also select regions where M_H is narrowly distributed. The peak of the magnitude PDF does not strongly depend on color or metallicity over the region where the PDF is narrow. These $M_H([(J - K_s)_0, Z])$ are combined with an overall offset of $\Delta M_H = 0.08$ to determine the distances for RC stars used in this paper.

ticular its metal-poor end dominate in the outer Galaxy (Bensby et al. 2011; Nidever et al. 2014; Hayden et al. 2015), in agreement with the scale lengths measured from the SEGUE data (Bovy et al. 2012c). But a more detailed and quantitative characterization of the radial behavior of the stellar populations does not yet exist. Exactly how the continuity in local disk thicknesses and the disjoint high- and low- $[\alpha/\text{Fe}]$ sequences in abundances can be reconciled in a consistent formation scenario is currently a mystery. The complex behavior of the radial scale lengths with abundance found by Bovy et al. (2012c), as opposed to the smooth variation of the vertical scale height, indicates that a thorough exploration of the radial profile of MAPs might hold the key to resolve this tension.

While the MW disk’s overall vertical stellar density profile was long thought to be the result of some type of heating, whether from satellites (e.g., Quinn et al. 1993; Abadi et al. 2003; Brook et al. 2004) or through radial migration (e.g., Sellwood & Binney 2002; Schönrich & Binney 2009; Minchev & Famaey 2010; Loebman et al. 2011), the possibility that (at least some part of) the stellar disk formed “upside-down” with its current thickness has recently gained favor (Bournaud et al. 2009; Stinson et al. 2013; Bird et al. 2013). The smooth continuum of disk thicknesses found by Bovy et al. (2012a,c) disfavors the satellite accretion and few-satellites-heating scenarios, because those would create a discrete thick-disk component (e.g., Martig et al. 2014). However, observational evidence to prefer either radial migration or upside-down formation is scant to date.

Radial migration of stars from well inside the MW has been proposed as a mechanism to create the thicker, $[\alpha/\text{Fe}]$ -enhanced stellar disk components in

the solar neighborhood. Radial migration approximately conserves the vertical action (Solway et al. 2012; Vera-Ciro & D’Onghia 2015). For outwardly migrating stars, the decreased gravitational pull in the outer disk leads to larger vertical excursions that for ensembles of stars should lead to flaring. Whether radial migration causes the whole stellar disk or its components to flare depends on which stars participate in the migration process. If all stars migrate similarly, then all co-eval populations should flare, but if only special subclasses are affected (e.g., stars with low vertical excursions), then the overall effect of migration on the vertical structure might be small. While the current suite of simulations by no means exhaustively covers the various migration scenarios and histories that may have occurred in the MW, current simulations do indicate that kinematic biases in the population of migrators are significant enough that little or no effect on the vertical structure of the disk should be expected (Minchev et al. 2012; Roškar et al. 2013; Vera-Ciro et al. 2014). Significant radial mixing, therefore, may well happen without leading to flaring while still having a large effect on, e.g., the present-day abundance distribution. However, for migration to be the *cause* of the thickness of the thicker-disk components in the MW, flaring of sub-populations must occur and determining whether individual MAPs flare vertically towards larger radii can discriminate among formation mechanisms for the thick-disk components.

That radial migration should and does play a large role in the evolution of the low- $[\alpha/\text{Fe}]$ populations is becoming increasingly clear. Radial migration provides a natural way to explain the observed lack of correlation between age and metallicity in the solar neighborhood (Edvardsson et al. 1993; Nordström et al. 2004) in the presence of a strong correlation between age and $[\alpha/\text{Fe}]$ (Haywood et al. 2013). The change in skew of the metallicity distribution from negative in the inner MW to positive in the outer MW (Hayden et al. 2015) can arise from migration. As for the thicker components, if this migration process is important for all low- $[\alpha/\text{Fe}]$ stars (not just a biased subset), it makes the generic prediction of an outward flaring disk.

In this paper we set out to comprehensively determine the stellar population structure of the Milky Way’s stellar disk. We do so by determining the radial and vertical profile of MAPs, using SDSS-III/APOGEE (Eisenstein et al. 2011; Majewski et al. 2015) data. The APOGEE data are complementary to the SEGUE data, because they provide much better radial coverage by using near-infrared observations of a large number of giants close to the Galactic midplane: the sample of red-clump giants used here spans the radial range $4 \text{ kpc} \lesssim R \lesssim 15 \text{ kpc}$. This radial coverage allows us to determine the radial profile of MAPs in detail: the data clearly require to go beyond the simple radial-exponential profile assumed by Bovy et al. (2012c) and all other previous analyses. The wide radial range combined with good vertical coverage ($0 \leq |Z| \lesssim 2 \text{ kpc}$) also makes it possible to measure any flaring of MAPs, providing an essential test of the predictions of radial migration. Finally, the high-resolution spectroscopic observations let us define MAPs with high-precision ($[\text{Fe}/\text{H}]$, $[\alpha/\text{Fe}]$) abundances, such that MAPs have no substantial contamination from neighboring MAPs. These better APOGEE data end up

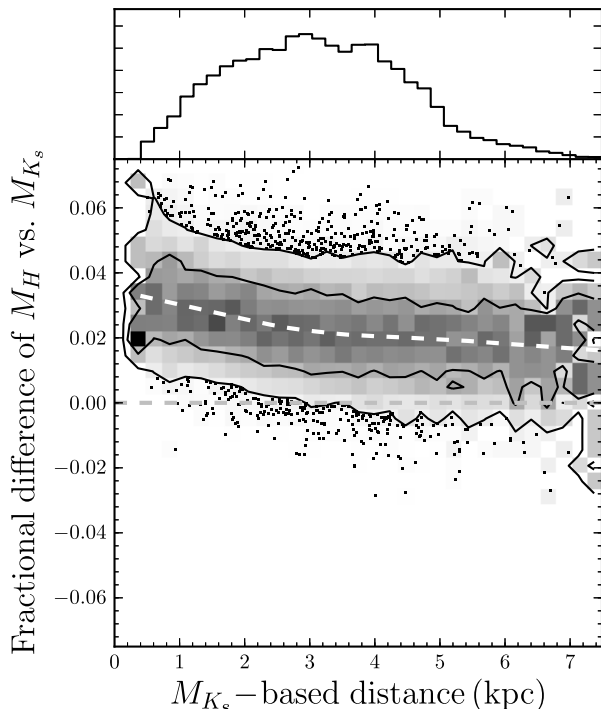


FIG. 3.— Fractional difference between the RC distances calculated based on the H -band and K_s -band luminosities as a function of the latter distance. The conditional distribution of distance differences is displayed for all 14,699 stars in the APOGEE-RC subsample used in this paper. The black contours contain 68 % and 95 % of the distribution and the white dashed line shows a lowess trendline. The overall median difference is only 2.3 %, consistent with the estimated $\approx 2\%$ systematic uncertainty in the RC distance scale (Bovy et al. 2014).

confirming the smooth, continuous distribution in scale height from the thinnest to the thickest disk components, as found by Bovy et al. (2012a).

The outline of this paper is as follows. In § 2 we present and discuss important aspects of the data from the APOGEE-RC catalog that this analysis is based on, paying particular attention to the abundance measurements in § 2.2. We describe the method for fitting the density profiles of stellar subsamples in APOGEE in § 3; this method is presented in more detail in Bovy et al. (2016). We apply the density-fitting methodology to broad abundance-selected subsamples in § 4 to explore the density profiles that represent the data well. In § 5 we then determine the density profiles of MAPs. We compare our results to previous work and discuss implications for our understanding of the formation and evolution of the MW disk in § 6. Finally, we present our conclusions in § 7. Readers not interested in the details of the data and fitting methodology are encouraged to skip to § 4. Throughout this paper, we assume that the Sun’s displacement from the mid-plane is 25 pc toward the North Galactic Pole (Chen et al. 2001; Jurić et al. 2008), and that the Sun is located at 8 kpc from the Galactic center.

2. DATA

2.1. APOGEE and the APOGEE-RC catalog

The SDSS-III/APOGEE (Majewski et al. 2015) is a high-resolution ($R \approx 22,500$) spectroscopic survey in the near-infrared (NIR; H -band; 1.51 to 1.70 μm). The survey employs a 300-fiber spectrograph (Wilson et al. 2010,

J. Wilson et al. 2016, in preparation) to obtain signal-to-noise ratio of 100 per half-resolution element (≈ 141 per resolution element) spectra for large numbers of stars in the Milky Way, observed during bright time on the 2.5-meter Sloan Foundation telescope (Gunn et al. 2006). The majority of APOGEE targets are selected from the 2MASS point-source catalog (Skrutskie et al. 2006), using a dereddened $(J - K_s)_0 \geq 0.5$ color cut in up to three magnitude bins in H (not corrected for extinction), with reddening corrections determined using the Rayleigh Jeans Color Excess method (RJCE; Majewski et al. 2011) applied to 2MASS and mid-IR data from Spitzer-IRAC GLIMPSE-I, -II, and -3D (Churchwell et al. 2009) when available and from WISE (Wright et al. 2010) otherwise. In this paper, we employ various three-dimensional extinction maps to take the effects of extinction on the observed H -band magnitude into account, but we always use the RJCE dereddenings for the $J - K_s$ color. A direct comparison between the 3D extinction maps and the RJCE extinctions exhibits good agreement between the two (see Bovy et al. 2016). Full details on the APOGEE target selection can be found in Zasowski et al. (2013). We use data from the SDSS-III Data Release 12 (DR12; Alam et al. 2015). The data processing (Nidever et al. 2015), stellar-parameters and chemical-abundances analysis (Shetrone et al. 2015; Zamora et al. 2015; García Pérez et al. 2015, and the DR12 data analysis and calibration (Holtzman et al. 2015) are performed with automated SDSS software; we make use of standard data products as contained in DR12.

Specifically, we base our analysis on red-clump (RC) star data from the DR12 APOGEE-RC catalog. This catalog consists of a pure sample of RC stars selected from the APOGEE catalog using the method described in detail by Bovy et al. (2014), but applied to the DR12 data (see Alam et al. 2015). RC stars are identified in the superset of all APOGEE data using a combination of cuts in the surface-gravity ($\log g$) / effective-temperature (T_{eff}) plane and the $(J - K_s)_0$ / metallicity ($[\text{Fe}/\text{H}]$) plane, chosen such as to select those RC stars for which precise luminosity distances can be determined. The catalog has an estimated purity of $\approx 95\%$; the distances are precise to 5 % and unbiased to 2 %. In order to account for biases due to the APOGEE target selection, we only use the subset of RC data that (a) was selected as part of the “main” APOGEE sample (defined using the $[J - K_s]_0 \geq 0.5$ color cut), and (b) are part of a line of sight and magnitude bin combination for which the planned APOGEE observations were complete in DR12, because these are the stars for which we can reconstruct the sample selection function. In our density-fitting methodology (see § 3 below) we correct for the effects of interstellar extinction using the 3D extinction maps of Marshall et al. (2006) in the inner-disk plane and Green et al. (2015) elsewhere (using $A_H/A_{K_s} = 1.48$ and $A_H/E(B - V) = 0.46$; Schlafly & Finkbeiner 2011; Yuan et al. 2013); the latter is based on Pan-STARRS and 2MASS data and does not cover the entire APOGEE footprint. We therefore remove 10 APOGEE fields that lie outside of the Green et al. (2015) footprint. These are the fields centered on $(l, b) = (240, -18)$, $(5.5, -14.2)$, $(5.2, -12.2)$, $(1, -4)$, $(0, -5)$, $(0, -2)$, $(358, 0)$, $(358.6, 1.4)$ (difficult

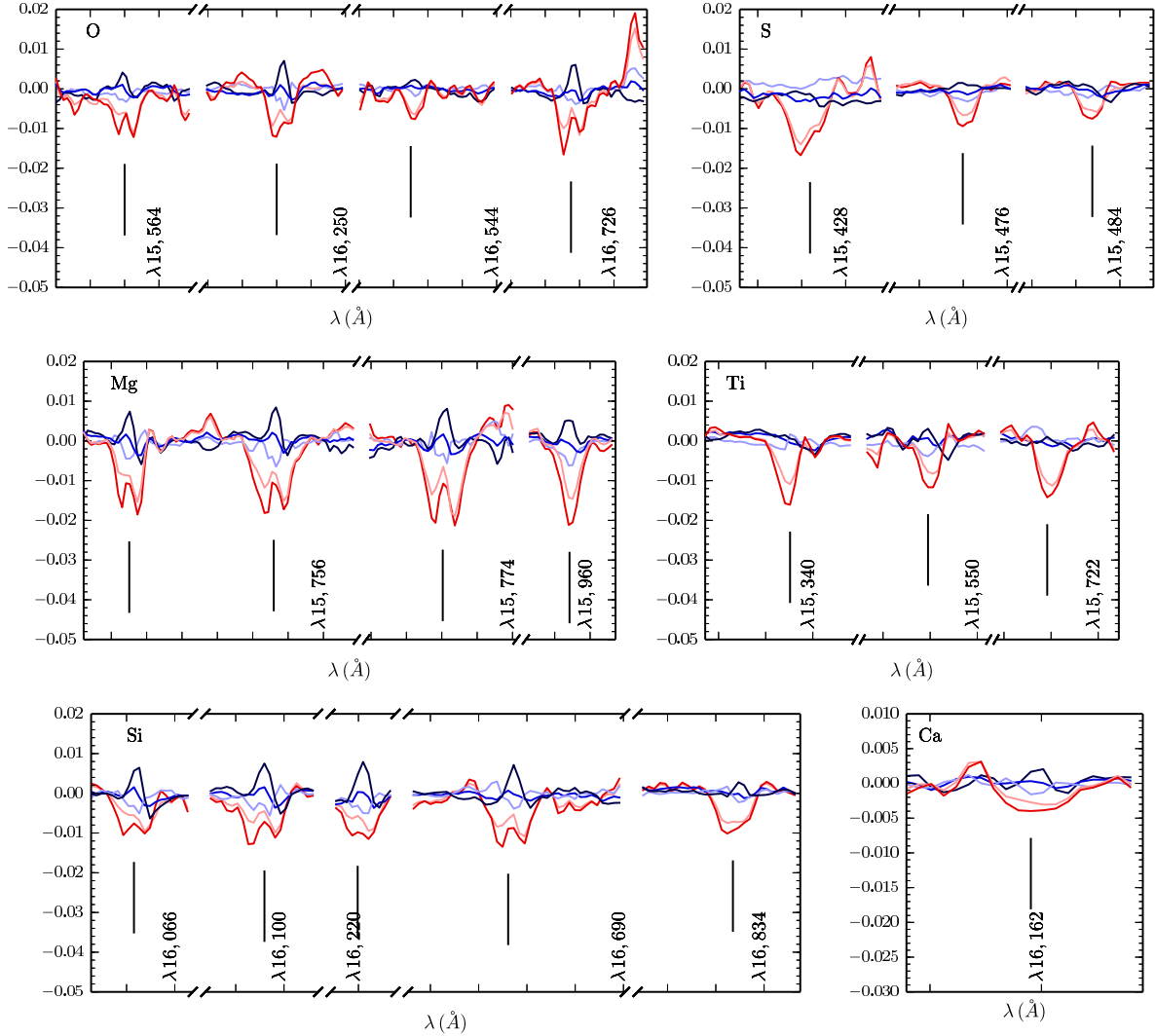


FIG. 4.— Directly apparent signatures of $[\alpha/\text{Fe}]$ variations among APOGEE-RC stars, split by individual alpha-elements. This figure illustrates spectral differences in wavelength regions with strong features due to O, Mg, Si, S, Ca, and Ti for stars over a narrow range in $[\text{Fe}/\text{H}]$ ($-0.45 < [\text{Fe}/\text{H}] \leq -0.35$). Each panel displays residuals from a mean spectrum after interpolating each spectral pixel to a common T_{eff} , $\log g$, and $[\text{Fe}/\text{H}]$ using quadratic interpolation. Residuals are smoothed by only including the part of the spectrum contained in the sub-space spanned by the eigenvectors of the eight largest PCA components of the residuals of all 490 stars in this $[\text{Fe}/\text{H}]$ range; this sub-space contains all of the variance above the measurement noise (we only include spectra with $S/N > 200$ in this figure). A stack of twelve random residuals each in five bins in $\Delta[\alpha/\text{Fe}] = [([O + \text{Mg} + \text{Si} + \text{S} + \text{Ca}]/5)/\text{Fe}] = 0.05$ —which does not include Ti (see text)—ranging from 0.00 (dark blue) to 0.20 (dark red) is displayed. The x axis only covers small parts of the full APOGEE spectral range in each panel and is interrupted in most panels to focus on features due to a specific element; the wavelength of the reddest tickmark in each section is indicated and the tickmark spacing is 2 \AA everywhere. The location of the spectral features for each element are indicated in each panel. Note that the scale for the Ca panel is different due to the weakness of the Ca feature. This figure demonstrates the high precision in $[\alpha/\text{Fe}]$ and the high level of consistency between the abundances of different α elements obtained from the H -band APOGEE spectra: $\sigma_{[\alpha/\text{Fe}]} \leq 0.02$ dex.

to access from the Northern Hemisphere) and $(l, b) = (120, 30), (123, 22.4)$. This only removes 125 stars. We further remove 13 stars with distance moduli based on their H -band luminosity (see below) < 8.49 , because they could not be in our sample if we model the RC as a standard candle with $M_H = -1.49$ (our standard assumption below). This statistical sample contains 14,699 RC stars. This sample spans a range $4500 \text{ K} \lesssim T_{\text{eff}} \lesssim 5200 \text{ K}$ and $2.25 \lesssim \log g \lesssim 3$ (95% ranges).

Figure 1 displays the sky distribution of the lines of sight included in the statistical RC sample, demonstrating the excellent coverage of the Galactic plane at low latitude. The fields are overlaid on the extinction map

to a distance of $D = 5 \text{ kpc}$ from Green et al. (2015) to illustrate the large amount of extinction affecting the disk region. While the distribution of fields includes a large number of fields in the region of the sky that contains the Galactic bulge, observations in these fields were limited to $H < 11$. Because the RC has $M_H \approx -1.49$, this implies that the bulge is not actually included in our sample (these fields have $D \lesssim 3 \text{ kpc}$); the coverage is primarily of the disk.

As discussed in detail in § 5 of Bovy et al. (2014), the overall-APOGEE and RC-specific selection cuts used to define the APOGEE-RC sample excludes stars with ages $\gtrsim 800 \text{ Myr}$ and metallicities $[\text{Fe}/\text{H}] \gtrsim -0.9$. The

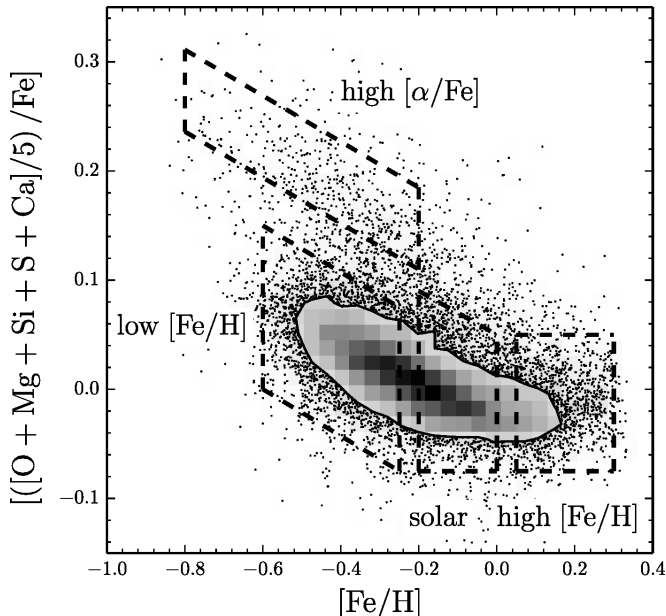


FIG. 5.— Distribution of the 14,699 stars in the APOGEE-RC sample used in this paper in the plane defined by the iron abundance, $[\text{Fe}/\text{H}]$, and the average abundance of α elements (see text). A linear binned density representation is used for the 68% of the distribution that is contained within the shown contour. The dashed lines delineate the boundaries of the four broad subsamples that we study in § 4, which we denote with the given moniker.

youngest part of the disk, as well as components more metal-poor than the bulk of the disk (e.g., Carollo et al. 2010) are therefore not represented in the sample; however, most of the disk mass satisfies these constraints. Because the RC consists of evolved giants stars that spend ≈ 100 Myr of their lifetime in the RC phase, the population of RC stars is a biased tracer of the underlying stellar populations in the Milky Way. The extent of this bias is primarily dependent on the metallicity and the (unknown) age distribution, but the dominant effect is that the APOGEE-RC selection overrepresents stars in the 1 to 4 Gyr age range with respect to the underlying age distribution. For example, for a relatively constant star-formation history, the APOGEE-RC selection is expected to be dominated by stars with ages between 1 and 4 Gyr, although older ages are represented at a lower level.

Distances for stars in the APOGEE-RC catalog are determined by combining corrections to a single absolute magnitude M_{K_s} , as a function of $([J - K_s]_0, [\text{Fe}/\text{H}])$, based on stellar-evolution models (Bressan et al. 2012); these corrections are applied to each individual star. The overall distance scale is calibrated against an *Hipparcos*-based determination of the RC absolute K_s magnitude in the solar neighborhood (Laney et al. 2012). In this paper, we determine distances based on the H -band luminosity rather than that in the K_s -band, because the APOGEE sample selection is performed in apparent H -band magnitude and our density-fitting formalism is simplest in this case. We follow the same procedure as discussed in §§ 2 and 3 of Bovy et al. (2014) to compute the corrections to a single H -band luminosity for the RC, as a function of $([J - K_s]_0, [\text{Fe}/\text{H}])^9$, and to calibrate the distance scale to the *Hipparcos* value of $M_H = -1.49$. The

absolute magnitude $M_H([J - K_s]_0, [\text{Fe}/\text{H}])$ is displayed in Figure 2. Figure 3 displays the fractional difference between the distances for stars in our sample determined from their K_s magnitude (the standard APOGEE-RC catalog product) and from their H magnitude. The fractional difference is $\lesssim 3\%$ for all stars, with a median of 2.3%. This is similar to the overall accuracy of the RC distance scale and so small that it does not impact the density fits below.

2.2. Abundance measurements and main subsamples

We make use of the abundance measurements provided in the DR12 release of APOGEE data (Holtzman et al. 2015). Specifically, we use the iron content, $[\text{Fe}/\text{H}]$, and the average abundance of α elements relative to iron. $[\text{Fe}/\text{H}]$ is measured from 64 iron lines in the H -band. As discussed by Holtzman et al. (2015), $[\text{Fe}/\text{H}]$ is internally corrected for trends with T_{eff} for stars in globular and open clusters observed by APOGEE. This internal calibration only amounts to differences of ≈ 0.04 dex over the ≈ 700 K spanned by the RC. We determine the precision in $[\text{Fe}/\text{H}]$ by comparing measurements of $[\text{Fe}/\text{H}]$ for different stars in the open clusters of Mészáros et al. (2013) in the T_{eff} range of the RC and find that $\sigma_{[\text{Fe}/\text{H}]} = 0.05$ dex.

We define the average α -enhancement as an average of the abundance of O, Mg, Si, S, and Ca. We do not include Ti, because of issues with its measurement in the H band (see Holtzman et al. 2015 for further discussion). Specifically, we average the abundances of $[\text{O}/\text{H}]$, $[\text{Mg}/\text{H}]$, $[\text{Si}/\text{H}]$, $[\text{S}/\text{H}]$, and $[\text{Ca}/\text{H}]$ and subtract $[\text{Fe}/\text{H}]$ to obtain the average α -enhancement $[\alpha/\text{Fe}]$. If no measurement was obtained for one of the five α elements, it is removed from the average. $[\text{O}/\text{H}]$ is measured from the abundant molecular OH and CO features in the near-infrared that are, however, relatively weak for the warm RC stars. Mg, Si, S, and Ca are measured from neutral atomic lines for two (Ca) to 12 (Si) features. The abundances of α elements are similarly corrected for trends with T_{eff} in clusters as $[\text{Fe}/\text{H}]$ above; for the average $[\alpha/\text{Fe}]$ as defined here, this calibration only gives differences of 0.03 dex over the ≈ 700 K spanned by the RC. We determine the empirical precision in $[\alpha/\text{Fe}]$ using the scatter in $[\alpha/\text{Fe}]$ for the calibration open clusters described above, and find that $\sigma_{[\alpha/\text{Fe}]} \approx 0.02$ dex, with a correlation of -0.4 with $[\text{Fe}/\text{H}]$.

We apply a simple external calibration of $[\text{Fe}/\text{H}]$ and $[\alpha/\text{Fe}]$ as follows. Using the APOGEE catalog abundances we determine the average $[\text{Fe}/\text{H}]$ and $[\alpha/\text{Fe}]$ for giants observed by APOGEE in the temperature range of the RC ($4500 \text{ K} < T_{\text{eff}} < 5200 \text{ K}$; see above) in M67, an open cluster that provides an excellent chemical solar analog (e.g., Önehag et al. 2014). We find that $[\text{Fe}/\text{H}]_{\text{M67}} = 0.10$ dex and $[\alpha/\text{Fe}]_{\text{M67}} = 0.03$ dex; the large offset in $[\text{Fe}/\text{H}]_{\text{M67}}$ is at least partly due to an incorrect line list used in DR12 (see Shetrone et al. 2015). To calibrate APOGEE closer to the solar abundance scale using M67, we apply constant offsets of -0.1 dex in $[\text{Fe}/\text{H}]$ and -0.05 dex in $[\alpha/\text{Fe}]$. The reason for applying an offset of -0.05 dex rather than -0.03 dex in $[\alpha/\text{Fe}]$ is that we define MAPs below using bins with

⁹ We convert the metallicity $[\text{Fe}/\text{H}]$ to metal mass fraction Z

assuming $Z_{\odot} = 0.017$ and solar abundance ratios.

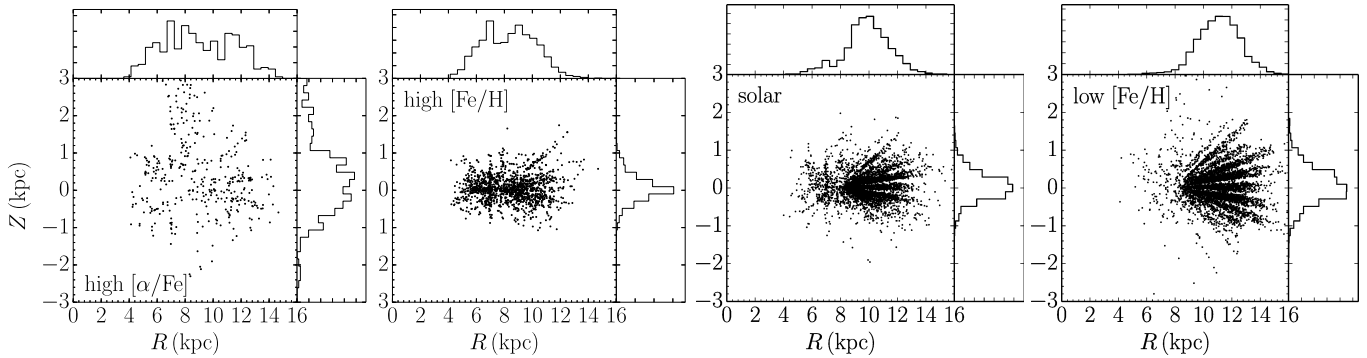


FIG. 6.— Observed spatial distribution of stars in the four broad subsamples defined in Figure 5, in Galactocentric radius, R , and distance from the mid-plane, Z . The Sun is located at $(R, Z) = (8, 0.025)$ kpc.

$\Delta[\alpha/\text{Fe}] = 0.05$ dex; a calibration offset of -0.05 dex therefore does not change the binning of the data, which is the same when using the catalog abundances or the externally-calibrated abundances defined here.

Figure 4 demonstrates the precision of our $[\alpha/\text{Fe}]$ abundances. This figure considers RC stars with $S/N > 200$ with $-0.35 < [\text{Fe}/\text{H}] \leq -0.25$. We interpolate the spectra for the 490 stars in our sample with these properties onto a common $T_{\text{eff}} = 4800$ K, $\log g = 2.85$ and $[\text{Fe}/\text{H}] = -0.3$, using quadratic interpolation. This removes the dominant effects of these stellar properties to reveal the effect of $[\alpha/\text{Fe}]$ on the spectra. We perform a PCA analysis of the residuals from a mean spectrum after the interpolation taking the measurement uncertainties into account (Bailey 2012), and only retain the components of each spectrum corresponding to the eight PCA eigenvectors with the largest eigenvalues. These eight eigenvectors explain all of the variance in the residuals above the measurement noise. Figure 4 displays median-stacked residuals of twelve random stars each in five bins in $[\alpha/\text{Fe}]$ with $\Delta[\alpha/\text{Fe}] = 0.05$ dex ranging from $[\alpha/\text{Fe}] = 0.00$ to $[\alpha/\text{Fe}] = 0.20$. We perform this median stacking of a small number of spectra to reduce the noise for display purposes. It is clear from this figure that we measure $[\alpha/\text{Fe}]$ at very high precision from the spectral lines of O, Mg, Si, S, and Ca. The relative abundances of these elements with respect to each other appear to have little variation.

Figure 5 displays the distribution of the statistical APOGEE-RC sampling in $([\text{Fe}/\text{H}], [\alpha/\text{Fe}])$. This distribution contains the two main sequences—high- and low- $[\alpha/\text{Fe}]$ —seen in other investigations of this distribution and discussed in detail for the APOGEE sample by Nidever et al. (2014) and Hayden et al. (2015). Also indicated in this figure are the four broad abundance-selected subsamples that we consider in § 4. The spatial distribution of stars in these four subsamples is displayed in Figure 6. With due caution about the effect of selection biases (which we correct for in the remainder of this paper) it is clear that the low- $[\alpha/\text{Fe}]$, low- $[\text{Fe}/\text{H}]$ stars are primarily found in the outer disk, while the higher- $[\text{Fe}/\text{H}]$ low- $[\alpha/\text{Fe}]$ stars are found closer to the center. High- $[\alpha/\text{Fe}]$ stars are found throughout the observed volume and are, in particular, more numerous at large distances from the mid-plane.

In § 5, we consider MAPs, defined in the same manner as in Bovy et al. (2012c) as stars in bins with $\Delta[\text{Fe}/\text{H}] = 0.1$ dex and $\Delta[\alpha/\text{Fe}] = 0.05$ dex. From the discussion of the uncertainties above, it is evident that the contamina-

tion between neighboring MAPs is slight, and that that between non-neighboring bins is essentially non-existent.

3. DENSITY-FITTING METHODOLOGY

3.1. Generalities

To fit the spatial density profile for subsamples of RC stars, we follow the methodology of Bovy et al. (2012c) (see also Rix & Bovy 2013), who model the observed rate of stars in the joint parameter space of position, magnitude, color, and metallicity using a Poisson process. Best-fit parameters and their uncertainties for parameterized spatial profiles are obtained by sampling this Poisson process’ likelihood of the observed data multiplied with an uninformative prior. As discussed by Bovy et al. (2014) and above, for the RC stars we determine the absolute magnitude M_H as a function of color $(J - K_s)_0$ and metallicity $[\text{Fe}/\text{H}]$; therefore, almost the same methodology for fitting the spatial profiles of RC stars applies here as was used by Bovy et al. (2012c) to analyze G dwarfs (whose absolute magnitude M_r was similarly determined from the color $(g - r)_0$ and $[\text{Fe}/\text{H}]$).

In the present application, we therefore model the rate function $\lambda(O|\theta)$ that is a function of $O = (l, b, D, H, [J - K_s]_0, [\text{Fe}/\text{H}])$, and is parameterized by parameters θ ; $\lambda(O|\theta)$ is given by

$$\begin{aligned} \lambda(O|\theta) = & \nu_*(X, Y, Z|\theta) \times |J(X, Y, Z; l, b, D)| \\ & \times \rho(H, [J - K_s]_0, [\text{Fe}/\text{H}]|X, Y, Z) \times S(l, b, H), \end{aligned} \quad (1)$$

where $\nu_*(\cdot|\theta)$ is the spatial density in Galactocentric rectangular coordinates (X, Y, Z) that we are ultimately most interested in and that depends on parameters θ , $|J(X, Y, Z; l, b, D)|$ is the Jacobian of the transformation between (X, Y, Z) and (l, b, D) , $\rho(H, [J - K_s]_0, [\text{Fe}/\text{H}]|X, Y, Z)$ is the density of stars in magnitude-color-metallicity space, and $S(l, b, H)$ is the survey selection function (the fraction of stars from the underlying population of potential targets observed by the survey). In APOGEE, the survey selection function is a function of position on the sky, is constant with (l, b) within an APOGEE field, and is a piecewise-constant function of apparent H -band magnitude, because targets were sampled in magnitude bins. The APOGEE selection function is determined, tested, and discussed in detail in § 4 of Bovy et al. (2014). For the present work, we have updated the selection function to the full three-year data set presented in DR12.

As in Bovy et al. (2012c), the rate has an additional

amplitude parameter. To remove this parameter from further consideration, we marginalize the probability of the parameters of the rate function over the amplitude of the rate. The marginalized likelihood can be written as

$$\mathcal{L}(\theta) = \sum_i \left[\ln \nu_*(X_i, Y_i, Z_i | \theta) - \ln \int dO \lambda(O | \theta) \right]. \quad (2)$$

In this expression, we have made use of the fact that the rate $\lambda(O_i | \theta)$ only depends on θ through $\nu_*(\cdot | \theta)$ and therefore the $\nu_*(X_i, Y_i, Z_i | \theta)$ is the only factor in $\lambda(O_i | \theta)$ that depends on θ ; the other factors can be dropped. The integral in this equation is the effective volume of the survey that provides the normalization of the rate likelihood. It does not depend on the individual data point, but is instead a property of the whole survey for a given model specified by θ .

Equation (2) is similar to the equivalent likelihood in Bovy et al. (2012c) (their equation [8]). The only significant difference between the two expressions is that the APOGEE selection function depends on the apparent magnitude H that is *not* corrected for extinction, while the SEGUE selection was performed in extinction-corrected magnitude. Therefore, to calculate the normalization integral in equation (2) we require a model for the three-dimensional distribution of extinction A_H to convert the model prediction's H_0 to H . We discuss the methodology for efficiently calculating the effective volume for different types of surveys in Bovy et al. (2016). For a pencil-beam survey like APOGEE, for which we can assume that the density is constant over the area of each field, the effective volume can be efficiently computed as

$$\int dO \lambda(O | \theta) = \sum_{\text{fields}} \Omega_f \int dD D^2 \nu_*([X, Y, Z](D, \text{location}) | \theta) \mathbf{S}(\text{location}, D), \quad (3)$$

where $\mathbf{S}(\text{location}, D)$ is the *effective selection function*. For APOGEE, this is given by

$$\mathbf{S}(\text{location}, D) = \sum_k S(\text{location}, k) \frac{\Omega(H_{\min, k} - H_0(D) < A_H(l, b, D) < H_{\max, k} - H_0(D))}{\Omega_f}, \quad (4)$$

where the sum is over the different magnitude bins, $[H_{\min, k}, H_{\max, k}]$, that stars are selected in along each line of sight. The numerator $\Omega(H_{\min, k} - H_0 < A_H(D) < H_{\max, k} - H_0)$ is the area of the APOGEE field in question, with A_H between the given boundaries, and the denominator Ω_f is the total area of the field. $S(\text{location}, k)$ is the APOGEE survey selection function, i.e., the fraction of potential targets with APOGEE spectroscopic observations in each magnitude bin. This equation assumes that the RC is a standard candle with $M_H = -1.49$, allowing us to compute $H_0(D)$. Bovy et al. (2016) demonstrate that this assumption does not affect the density

measurements here.

3.2. Stellar Number-density Models

We fit a variety of models for the stellar number density of abundance-selected populations. All of the models for which results are given in this paper assume that the density is axisymmetric and that the radial profile is separable from the vertical profile, such that

$$\nu_*(R, \phi, Z) = \Sigma(R) \zeta(Z), \quad (5)$$

where we define $\zeta(Z)$ such that $\int dZ \zeta(Z) = 1$. We have performed fits that add a constant density to capture any outliers, but find that the contribution from outliers is negligible in all cases; therefore we do not include them in this description. The basic model for $\Sigma(R)$ that we consider here is that of a broken exponential

$$\ln \Sigma(R) \propto \begin{cases} -h_{R, \text{in}}^{-1} (R - R_0) & R \leq R_{\text{peak}}, \\ -h_{R, \text{out}}^{-1} (R - R_0) & R > R_{\text{peak}}. \end{cases} \quad (6)$$

The relative normalization of these exponentials is set to produce a continuous $\Sigma(R)$ at R_{peak} . In MCMC explorations of the parameter constraints, the inverse scale lengths and the logarithm of R_{peak} are given flat priors. We also consider models where $\Sigma(R)$ is a single exponential; such models essentially have $R_{\text{peak}} \equiv 0$.

We have explored additional functional forms for $\Sigma(R)$, such as a Gaussian centered on R_{peak} , but find that the density is typically best described as a broken exponential. However, because the density drops quickly as one moves away from R_{peak} , and because the disk has a large range of R_{peak} (see below), determining the exact form of the radial profile is difficult with the current data.

We consider four distinct functional forms for $\zeta(Z)$. The first is that of a single exponential, with a scale height that is an exponential function of radius R (i.e., a flaring model)

$$\ln \zeta(Z) \propto h_Z^{-1} \exp(R_{\text{flare}}^{-1} [R - R_0]) |Z|. \quad (7)$$

To investigate the flaring profile further, we also consider non-exponential flaring that is either linear or inverse-linear, i.e.

$$\ln \zeta(Z) \propto h_Z^{-1} (1 \pm R_{\text{flare}}^{-1} [R - R_0])^{\pm 1} |Z|, \quad (8)$$

where the signs are such that R_{flare}^{-1} is always negative for outwardly-increasing h_Z . In MCMC explorations of the PDF, the inverse scale height h_Z^{-1} and the inverse flaring scale length R_{flare}^{-1} are given uniform priors. A non-flaring vertical profile has $R_{\text{flare}}^{-1} = 0$. The second form for $\zeta(Z)$ is a sum of two exponentials

$$\zeta(Z) = \frac{1 - \beta_2}{2 h_Z} \exp(h_Z^{-1} |Z|) + \frac{\beta_2}{2 h_{Z,2}} \exp(h_{Z,2}^{-1} |Z|). \quad (9)$$

We also briefly consider the generalization of the models in equations (7) and (9), i.e., the two-exponential model where each scale height flares exponentially as in equation (7). As demonstrated below, the two-exponential form for the vertical profile does not fit the data as well as the flaring single-exponential form. Our main use of the second form is to investigate whether any MAPs show evidence of a secondary component with a different scale height.

TABLE 1
RESULTS FOR BROAD ABUNDANCE-SELECTED SAMPLES

Sample	Density model	Extinction map	$h_{R,\text{in}}^{-1}$ (kpc $^{-1}$)	$h_{R,\text{out}}^{-1}$ (kpc $^{-1}$)	R_{peak} (kpc)	h_Z (kpc)	R_{flare}^{-1} or β_2 (kpc $^{-1}$ or -)	$h_{Z,2}$ (kpc)	$\Delta\chi^2$
low [Fe/H] (low $[\alpha/\text{Fe}]$)	broken exp. w/ flare	Marshall et al. (2006)	0.27 ± 0.03	0.36 ± 0.11	10.8 ± 0.1	0.37 ± 0.02	-0.09 ± 0.01	...	0
		Green et al. (2015)	0.28	0.37	10.8	0.38	-0.08	...	13
		Sale et al. (2014)	0.28	0.37	10.8	0.38	-0.08	...	91
		Drimmel et al. (2003)	0.27	0.45	10.9	0.37	-0.10	...	649
		zero	0.34	0.59	10.9	0.39	-0.10	...	2162
	single exp. broken exp. w/ 2 h_Z	Marshall et al. (2006)	...	0.06 ± 0.01	...	0.45 ± 0.01	723
		Marshall et al. (2006)	0.28 ± 0.03	0.37 ± 0.02	10.8 ± 0.1	0.47 ± 0.01	< 0.01	0.19 ± 97.44	74
	solar (low $[\alpha/\text{Fe}]$)	Marshall et al. (2006)	0.09 ± 0.04	0.65 ± 0.02	9.2 ± 0.1	0.28 ± 0.01	-0.09 ± 0.01	...	0
		Green et al. (2015)	0.15	0.65	9.2	0.29	-0.08	...	77
		Sale et al. (2014)	0.15	0.65	9.2	0.29	-0.08	...	149
		Drimmel et al. (2003)	0.07	0.71	9.4	0.29	-0.09	...	286
		zero	0.29	0.78	9.3	0.32	-0.07	...	1443
high [Fe/H] (low $[\alpha/\text{Fe}]$)	single exp. broken exp. w/ 2 h_Z	Marshall et al. (2006)	...	0.33 ± 0.01	...	0.31 ± 0.01	906
		Marshall et al. (2006)	0.11 ± 0.03	0.66 ± 0.02	9.2 ± 0.1	0.33 ± 0.01	< 0.01	0.11 ± 29.94	90
	broken exp. w/ flare	Marshall et al. (2006)	0.28 ± 0.15	0.81 ± 0.03	6.8 ± 0.2	0.27 ± 0.01	-0.14 ± 0.02	...	0
		Green et al. (2015)	0.62	0.79	6.5	0.28	-0.12	...	98
		Sale et al. (2014)	0.56	0.79	6.6	0.28	-0.12	...	148
		Drimmel et al. (2003)	0.20	0.81	6.8	0.28	-0.14	...	84
		zero	1.07	0.78	6.5	0.30	-0.10	...	832
	single exp. broken exp. w/ 2 h_Z	Marshall et al. (2006)	...	0.60 ± 0.01	...	0.28 ± 0.01	430
		Marshall et al. (2006)	0.43 ± 0.32	0.80 ± 0.08	6.6 ± 1.7	0.28 ± 0.01	< 0.02	0.09 ± 1.66	95
high $[\alpha/\text{Fe}]$	broken exp. w/ flare	Marshall et al. (2006)	0.93 ± 0.57	0.43 ± 0.03	< 4.4	0.95 ± 0.05	0.01 ± 0.03	...	0
		Green et al. (2015)	1.16	0.43	1.0	0.97	0.02	...	6
		Sale et al. (2014)	0.95	0.43	1.8	0.97	0.02	...	10
		Drimmel et al. (2003)	0.88	0.45	4.1	0.96	0.00	...	14
		zero	0.00	0.40	1.1	1.09	0.04	...	170
	single exp. broken exp. w/ 2 h_Z	Marshall et al. (2006)	...	0.43 ± 0.02	...	0.95 ± 0.05	0
		Marshall et al. (2006)	0.90 ± 0.57	0.43 ± 0.02	2.2 ± 1.2	0.95 ± 0.06	< 0.02	0.15 ± 195.28	0

NOTE. — Lower limits are at 95% posterior confidence. The seventh column is R_{flare}^{-1} for the flaring model and the amplitude β_2 for the model with two vertical scale heights. The parameters β_2 and $h_{Z,2}$ are marginalized under the constraint that $h_{Z,2}$ is 50% different from h_Z (to avoid the massive degeneracy when h_Z and $h_{Z,2}$ are allowed to be the same). The model consisting of a broken radial exponential with a flaring exponential scale height provides the best fit in all cases, although the high- $[\alpha/\text{Fe}]$ sample is always fit as a single radial exponential.

We optimize the likelihood in equation (2) for each density model and each data set below using a downhill simplex algorithm. We then use this optimal solution to initiate an MCMC sampling of the posterior PDF, obtained using an affine-invariant ensemble MCMC sampler (Goodman & Weare 2010; Foreman-Mackey et al. 2013). Reported parameter estimates are based on the median and standard deviation of one-dimensional projections of the MCMC chain.

3.3. Tests on mock data

We have performed a suite of mock-data tests to validate our code (i.e., checking that we recover the correct input density profiles when fitting a model that includes the input assumptions) and to determine the impact of the uncertainty in the three-dimensional extinction map. We generate mock data with profiles similar to a few of the best-fit profiles for the broad abundance-selected subsamples below. In particular, we produce mock data with a flat radial profile, a single-exponential profile with a scale length of 3 kpc, or broken-exponential profiles with peak radii of 8 and 11 kpc; all mock data have a constant thickness with a scale height of 300 pc, except that we also generate mock data with the exponential flaring profile of equation (7) with a scale length of 10 kpc for the broken-exponential profiles. All mock data assume extinction according to the Green et al. (2015) map and properly take into account the variation of the density profile within each APOGEE field, therefore testing that this can be ignored in the calculation of the effective volume (see above). Each mock-data sample has 20,000 stars.

When fitting the mock data with profiles that include the input density profile, we find that our code recovers the correct profile to within the uncertainties that we find for the real data below. In particular, we confirm that radial profiles consisting of a single exponential are

recovered as such, even when fit with more the general broken-exponential profile. Furthermore, we recover that no constant-scale-height mock data set displays any flaring and that the flaring scale length is correctly recovered in the mocks with flaring. For the latter, we also find that the radial profile is almost perfectly recovered even when they are fit with a constant scale height. This confirms the expectation that the radial and vertical profiles are measured almost independently of each other due to the many lines of sight at $b = 0^\circ$ in the APOGEE footprint (see Figure 1).

To determine the impact of the uncertainty in the interstellar extinction, especially in the inner MW, we fit the mock data assuming extinction according to Marshall et al. (2006) near the mid-plane, rather than the Green et al. (2015) extinction assumed in generating the mock data; the latter is typically smaller than the former. We find only small changes in the best-fit parameters when using the incorrect extinction map; these differences are smaller or similar to the uncertainties in the best-fit parameters, and do not lead to qualitatively-different inferred density profiles. Even employing the map of Drimmel et al. (2003) in the fit only changes the best-fit parameters by insignificant amounts, similar to what we find for the real data below. Therefore, we conclude that the uncertainty in the three-dimensional extinction does not limit our understanding of the spatial density profiles of stellar subsamples in APOGEE.

4. THE SPATIAL STRUCTURE OF BROAD ABUNDANCE-SELECTED SUBSAMPLES

We now discuss the results from fitting the spatial density of the broad abundance-selected subsamples (Figures 5 and 6), using the functional forms described in § 3.2 above. We start by fitting broad sub-samples first, because of the (relatively) large sample size that allows us to precisely determine the shape of their density profiles.

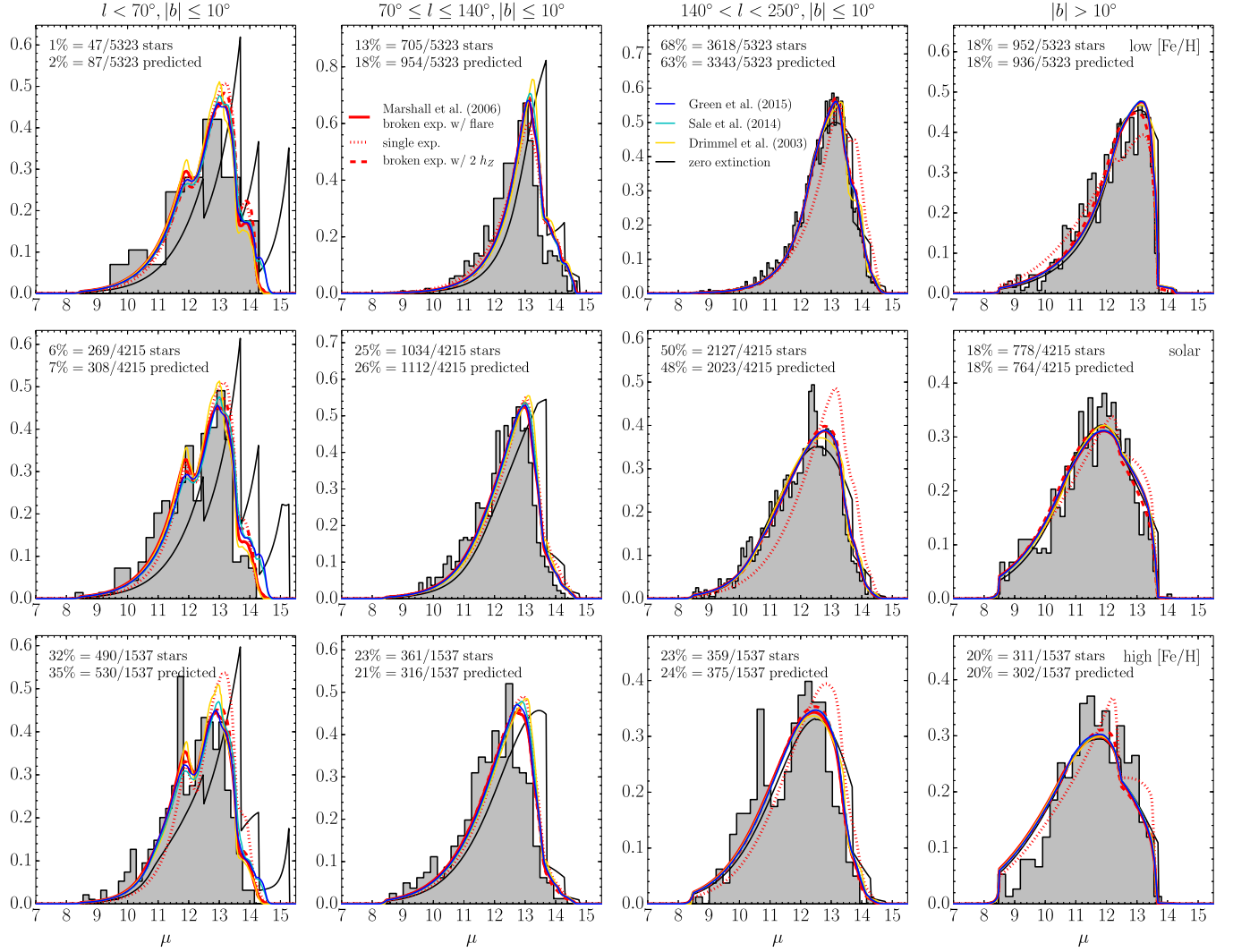


FIG. 7.— Comparison between the observed (filled histogram) distribution of distance moduli, μ , and that predicted by the best-fit models for the three low- $[\alpha/\text{Fe}]$ subsamples of Figure 5 (rows) and different regions of the sky (columns). The red curves demonstrate the fits using a combination of the Marshall et al. (2006) and Green et al. (2015) 3D extinction maps for the different density profiles displayed in Table 1. The remaining curves display the fits assuming different 3D extinction maps. The predicted number of stars in each spatial region is given for the fiducial model (broken exp. w/ flare with Marshall et al. 2006 extinction). Different 3D extinction maps give by and large similar fits, except for in the inner Galaxy (left panels), where the Marshall et al. (2006) map performs best. A model with zero extinction (black curves) provides poor fits for all low Galactic latitude locations. The sharp features in the zero-extinction model reflect the discontinuous nature of the APOGEE selection function as a function of H ; these are smoothed by the extinction for models with extinction (see Figure 6 in Bovy et al. 2016). The density in all cases is best fit as a radially broken exponential with a flaring vertical scale height; a single radial exponential fails to explain the radial profile over all radii, demonstrated by the poor fit in the outer regions of the disk (third panels).

In § 5 we then refine our results by fitting the preferred models from this section to the MAPs, which have much smaller sample sizes. The well-populated broad subsamples also make it possible to demonstrate the goodness of the fits of different spatial profiles by directly overlaying the best-fit models on the observed distribution of stars.

4.1. The surface-density profile

Results from fitting the density profiles given in § 3.2 to the broad abundance-selected subsamples are given in Table 1. Comparisons between different model fits discussed below and the observed distance distribution are displayed in Figure 7 for the three low- $[\alpha/\text{Fe}]$ subsamples, and in Figure 8 for the high- $[\alpha/\text{Fe}]$ subsample. We fit the radial and vertical profiles simultaneously, but fo-

cus on discussing the resulting radial profiles $\Sigma(R)$ in this subsection.

It is clear from Table 1 and Figure 7 that a single-exponential radial profile $\Sigma(R)$ (dotted line in Figure 7) does not provide a good fit to the data for the low- $[\alpha/\text{Fe}]$ subsamples. A broken exponential of the type as in equation (6) provides a much better fit. Discrepancies between the observed and predicted distribution of distances in Figure 7 are small for this model. In addition to the broken-exponential model, we have also performed fits with a Gaussian radial profile. These only gave similar or worse fits to the data, but with $\Delta\chi^2$ of only tens. The exact shape of the radial profile can therefore not be determined at high confidence, but it is clear that $\Sigma(R)$ for the low $[\alpha/\text{Fe}]$ subsamples increases up to a peak

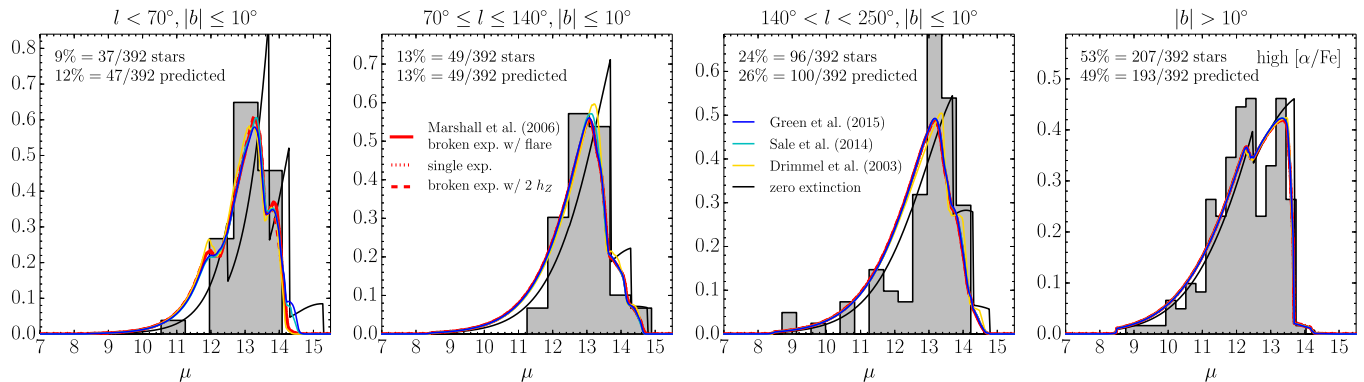


FIG. 8.— Same as Figure 7, but for the high- $[\alpha/\text{Fe}]$ sample. All different density profiles provide equally good fits, demonstrating that the density is very close to a single radial and vertical exponential for this population.

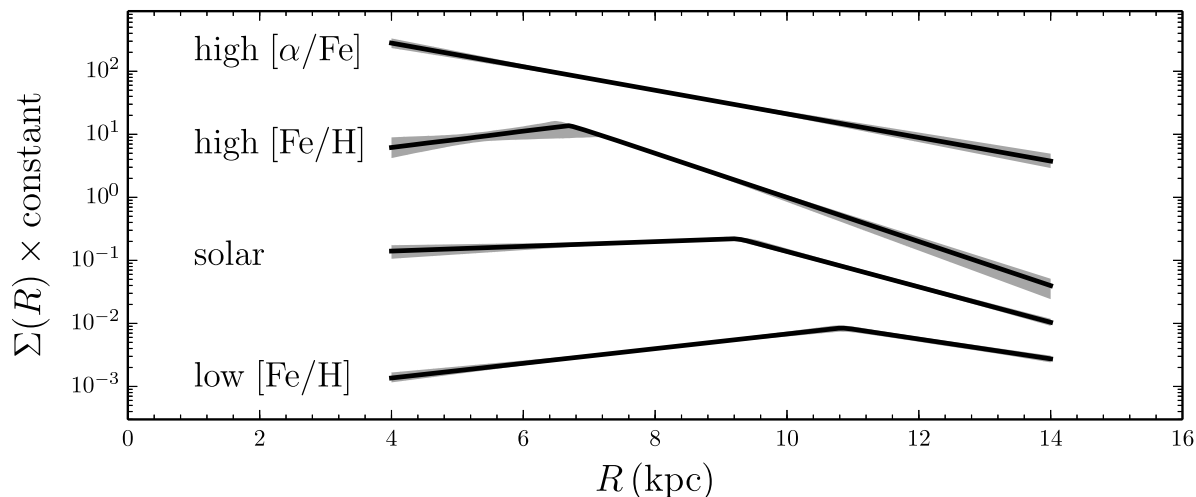


FIG. 9.— Radial surface profile $\Sigma(R)$ of the four broad abundance-selected subsamples indicated in Figure 5. The gray region gives the 95% uncertainty range. All profiles are relative to the density at $R = 8$ kpc; an arbitrary offset in the vertical direction has been applied to separate the four profiles. The three low- $[\alpha/\text{Fe}]$ subsamples are best represented as a broken exponential, while the high- $[\alpha/\text{Fe}]$ subsample consists of a single exponential distribution over the full radial range that is observed.

radius R_{peak} and declines beyond that. $\Sigma(R)$ is highly inconsistent with being a single exponential.

For the high- $[\alpha/\text{Fe}]$ subsample the single-exponential model provides a good fit, while fits with a broken-exponential or other radial profile all end up as close to a single exponential as possible. For example, the broken-exponential fit places R_{peak} outside of the observed volume ($R_{\text{peak}} < 4.4$ kpc; Table 1) such that this fit is equivalent to a single exponential. The Gaussian radial profile does the same, and adjusts the width parameter such that the profile closely approximates a single exponential. We can therefore be confident that $\Sigma(R)$ for the high- $[\alpha/\text{Fe}]$ subsample is very close to a single exponential.

The fits in Table 1 and Figures 7 and 8 are performed for several different extinction maps. The standard extinction map used is that of Green et al. (2015). Used on its own it is labeled as “Green et al. (2015)”. When we replace the part of it at $-100^\circ \leq l \leq 100^\circ$ and $|b| \leq 10^\circ$ with the map of Marshall et al. (2006), we label this as “Marshall et al. (2006)”; Likewise, when we replace the part of it that overlaps with the map of Sale et al. (2014), we refer to that model as “Sale et al. (2014)”. We also test the performance of two other extinction maps: that of Drimmel et al. (2003), which is defined over the entire

sky, and a model without any extinction (labeled “zero”).

In all cases the combination of the Marshall et al. (2006) and the Green et al. (2015) maps provides the best fit. The map of Sale et al. (2014) performs slightly worse than that of Green et al. (2015) where Sale et al. (2014) overlaps the latter. The map of Drimmel et al. (2003), which consists of a simple model for the three-dimensional distribution of dust and has lower angular resolution than the other maps, gives very poor fits. The model with zero extinction clearly provides a bad fit to the data, both from the $\Delta\chi^2$ in Table 1, and directly from the comparison between the model and the data in Figure 7, especially at $l < 70^\circ$. All of the different extinction maps, however, give very similar best-fit parameters for the basic model for the spatial density.

The radial profile and its uncertainties for the standard model of a broken exponential for the four broad subsamples is displayed in Figure 9. It is clear that the uncertainty in this (parametric) model is small, and that the peak radius R_{peak} for the low- $[\alpha/\text{Fe}]$ subsamples is larger for decreasing $[\text{Fe}/\text{H}]$. The shape of the radial profile around R_{peak} is quite similar for all three low- $[\alpha/\text{Fe}]$ subsamples, with a shallow rise at $R < R_{\text{peak}}$ and a steep decline at $R > R_{\text{peak}}$. The high- $[\alpha/\text{Fe}]$ subsample could be thought of as having $R_{\text{peak}} \lesssim 4$ kpc, and therefore be

the continuation of the trend of the low- $[\alpha/\text{Fe}]$ subsamples, but with the current radial coverage we cannot test that scenario.

4.2. The vertical profile

Having determined that a broken-exponential $\Sigma(R)$ provides the best fit, we fit three different vertical profiles to the APOGEE-RC data. The simplest model is that of a single-exponential model with a radially constant scale height h_z . By fitting more complex models, we find that this model is strongly ruled out for the low- $[\alpha/\text{Fe}]$ subsamples. They are instead better fit with a model where h_z is a function of R , and we employ the flaring model of equation (7) (the flaring profile is explored in more detail for the MAPs below using the alternative flaring models). An alternative model is that each subsample consists of the sum of two exponentials (the model of equation [9]); this model does not fit as well (see Table 1). We have also fit a generalized model where the vertical profile consists of the sum of two exponentials that flare exponentially with the same scale length. In all cases, the best fit for this general model reverts to that of the single-exponential, flaring model. All of the low- $[\alpha/\text{Fe}]$ subsamples are consistent with a common flaring scale length of $R_{\text{flare}}^{-1} \approx -0.1 \text{ kpc}^{-1}$. We refine this measurement in § 5.2 below.

Like for the surface-density profile, the high- $[\alpha/\text{Fe}]$ subsample is consistent with the simplest model, in this case a single vertical exponential with a constant $h_z(R)$. That is, we see with high confidence that the high- $[\alpha/\text{Fe}]$ subsample does not display the same kind of flaring as the low- $[\alpha/\text{Fe}]$ subsamples, but $h_z(R)$ is instead constant. We refine the quantitative constraint in § 5.2 below.

5. THE SPATIAL STRUCTURE OF MAPS

In this section we repeat the density fits from the previous section, but we perform them on abundance-selected subsamples that are narrower in $[\text{Fe}/\text{H}]$ and $[\alpha/\text{Fe}]$. That is, we use MAPs, defined here as abundance bins with widths of $\Delta[\text{Fe}/\text{H}] = 0.1 \text{ dex}$ and $\Delta[\alpha/\text{Fe}] = 0.05 \text{ dex}$. We do not make use of other abundances for defining MAPs, but stress that our empirical description does not assume chemical homogeneity beyond $([\text{Fe}/\text{H}], [\alpha/\text{Fe}])$. As discussed at the end of § 2.2, these widths are about twice as large as the uncertainties in these quantities and the contamination between MAPs is therefore small. Because of the small number of stars in the statistical APOGEE-RC at high $[\alpha/\text{Fe}]$, we perform fits for MAPs with at least 15 stars; the measurements for MAPs with so few stars are noisy, but informative enough to help establish trends. We again discuss the results for the surface-density and vertical profiles separately, but both were measured simultaneously for all MAPs.

5.1. The surface-density profile

Inspired by the fits to the broad abundance-selected subsamples in § 4.1, we fit a broken-exponential $\Sigma(R)$ to each well-populated MAP. We constrain these broken-exponential models to have an inner profile that is increasing with R and an outer profile that is decreasing, although the vast majority of MAPs have well constrained profiles without this prior constraint that satisfy it. For MAPs that are best fit as a single exponential,

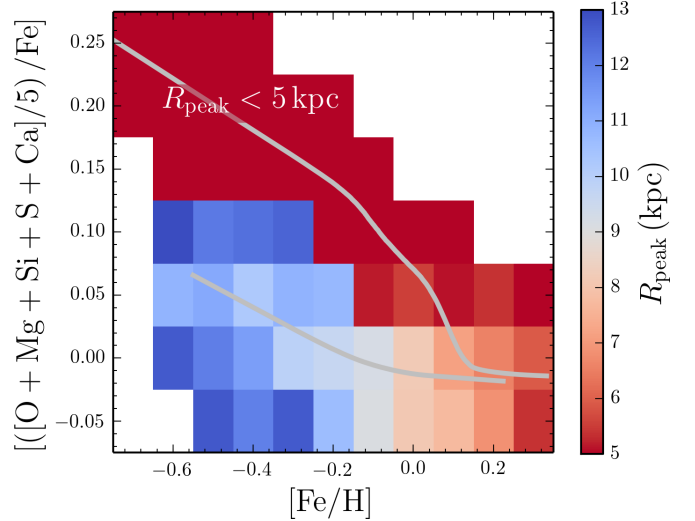


FIG. 10.— Peak radius of the radial profiles of MAPs. This figure displays the Galactocentric radius at which the surface density of each MAP peaks when fit with a broken-exponential radial profile that is constrained to be increasing within R_{peak} . The locus of the high- and low- $[\alpha/\text{Fe}]$ sequences in Figure 5 are indicated with gray curves. MAPs along the high- $[\alpha/\text{Fe}]$ sequence do not display a peak in their radial profile within the observed R range; they are best represented as a single radial exponential and are indicated as “ $R_{\text{peak}} < 5 \text{ kpc}$ ”. MAPs along the low- $[\alpha/\text{Fe}]$ sequence show a striking increase in R_{peak} with decreasing $[\text{Fe}/\text{H}]$.

this constraint forces R_{peak} to lie at small R ; without this constraint, the fit would have a degeneracy between very small R_{peak} and very large R_{peak} (as long as R_{peak} is outside of the observed volume). We always use the combined Marshall et al. (2006) and Green et al. (2015) extinction map, which provided the best fit to the broad subsamples above.

We display the dependence on $([\text{Fe}/\text{H}], [\alpha/\text{Fe}])$ of the peak of $\Sigma(R)$ in Figure 10. We determine R_{peak} typically to 0.3 kpc, while the range of R_{peak} covers about 8 kpc. Thus, the smooth trends seen in Figure 10 are determined at high significance. These more detailed results confirm the behavior found for the broad subsamples in § 4.1. Low- $[\alpha/\text{Fe}]$ MAPs have an increasing R_{peak} with decreasing $[\text{Fe}/\text{H}]$, ranging from $R_{\text{peak}} \approx 5 \text{ kpc}$ at the highest $[\text{Fe}/\text{H}]$, to $R_{\text{peak}} \approx 13 \text{ kpc}$ at the lowest $[\text{Fe}/\text{H}]$. This trend has a weak dependence on $[\alpha/\text{Fe}]$. We have indicated the locus where the low- $[\alpha/\text{Fe}]$ sequence is well populated (that is, where R_{peak} is best determined) and along this sequence the correlation between $[\text{Fe}/\text{H}]$ and R_{peak} is incredibly tight.

The behavior of individual high- $[\alpha/\text{Fe}]$ MAPs also confirms that high- $[\alpha/\text{Fe}]$ MAPs do not display a break in their surface-density profiles, but are instead consistent with a single exponential. For all MAPs along the high- $[\alpha/\text{Fe}]$ sequence, R_{peak} is constrained to lie outside of the observed volume.

The radial dependence of $\Sigma(R)$ is displayed in Figure 11. This figure only shows MAPs along the well-populated high- and low- $[\alpha/\text{Fe}]$ sequences for clarity, but the behavior of other MAPs is similar, albeit noisier. It is clear that the radial profiles for all but the lowest $[\text{Fe}/\text{H}]$ MAP are well constrained to have the broken-exponential form with an almost universal shape around R_{peak} . The inner profile is typically shallower than the outer profile, except for lower- $[\text{Fe}/\text{H}]$ MAPs. However, these MAPs

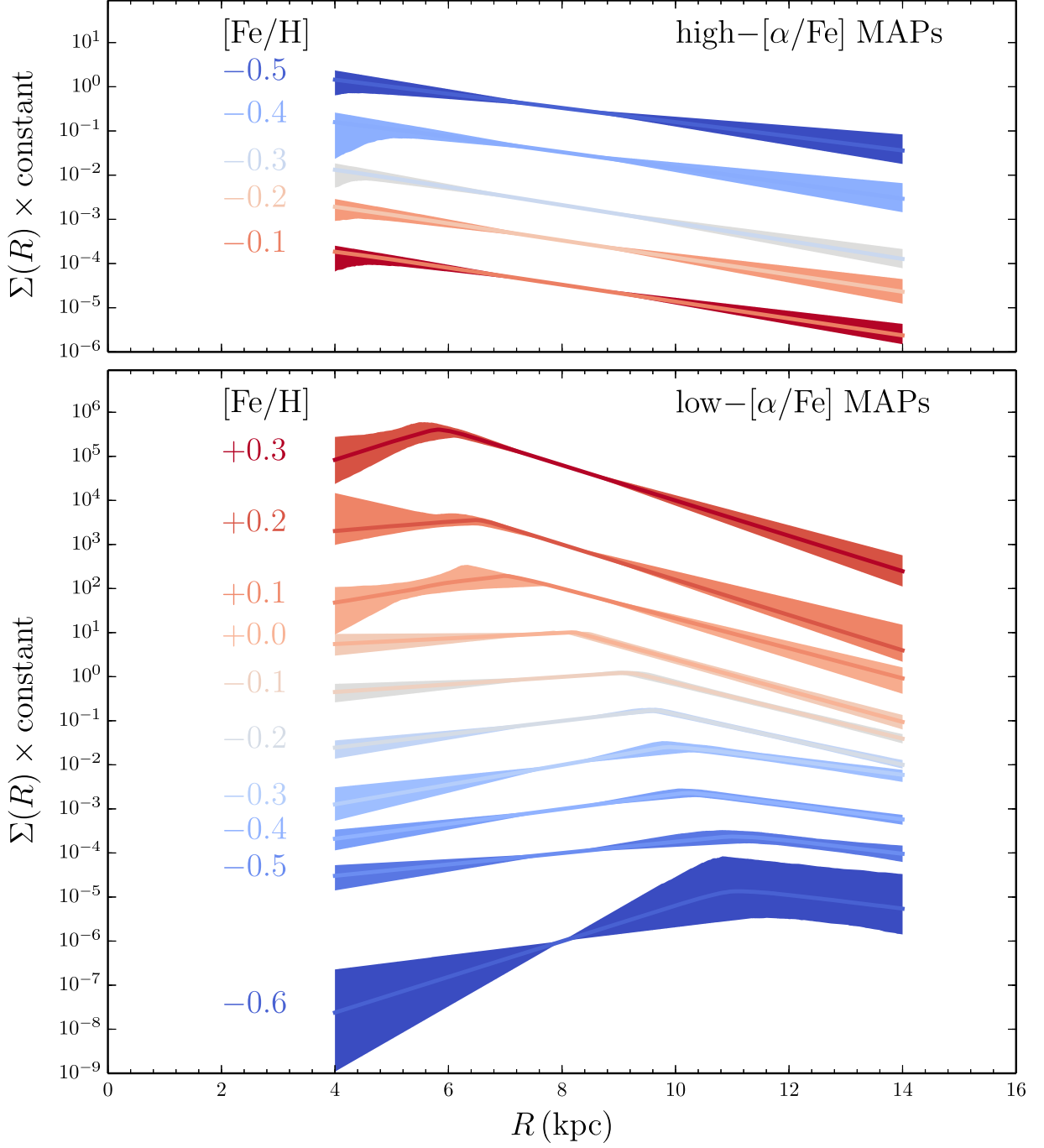


FIG. 11.— Radial surface profile of MAPs. For display purposes, MAPs along the well-populated low- and high- $[\alpha/\text{Fe}]$ sequences are shown in the bottom and top panel, respectively, but the trends are the same for all MAPs. For the low- $[\alpha/\text{Fe}]$ sequence these are the MAPs with $[\alpha/\text{Fe}] = +0.05$ up to $[\text{Fe}/\text{H}] = -0.4$ and $[\alpha/\text{Fe}] = 0.0$ at higher $[\text{Fe}/\text{H}]$. For the high- $[\alpha/\text{Fe}]$ sequence these are the MAPs with $[\alpha/\text{Fe}] = +0.20$ for $[\text{Fe}/\text{H}] = (-0.5, -0.4)$, $[\alpha/\text{Fe}] = +0.15$ for $[\text{Fe}/\text{H}] = (-0.3, -0.2)$, and $[\alpha/\text{Fe}] = +0.10$ for $[\text{Fe}/\text{H}] = -0.1$. The colored bands give the 95% uncertainty region. The radial profiles of high- $[\alpha/\text{Fe}]$ MAPs are given by single exponentials with a common scale length of 2.2 ± 0.2 kpc. The metal-poor low- $[\alpha/\text{Fe}]$ MAPs peak in the outer disk ($R_{\text{peak}} \gtrsim 10$ kpc) and are spread over a wide range of radii, with a relatively shallow outer scale length of about 3 kpc. The metal-rich low- $[\alpha/\text{Fe}]$ MAPs are very centrally-concentrated ($R_{\text{peak}} \lesssim 8$ kpc), with outer scale lengths of only ≈ 1.25 kpc. The inner, rising scale length is universally ≈ 3 kpc, in all MAPs where it can be constrained.

are only sparsely populated at the large distance from the Galactic center where their outer profiles are constrained, as is also evident from the uncertainties. The top panel displays $\Sigma(R)$ for the high- $[\alpha/\text{Fe}]$ MAPs. In addition to all being consistent with a single exponential, they are all consistent with *the same* single exponential,

with a scale length of $h_R = 2.2 \pm 0.2$ kpc.

5.2. The vertical profile

Results from fitting the MAPs with the standard model for the vertical density—a single exponential with an exponentially-increasing scale height—are displayed in

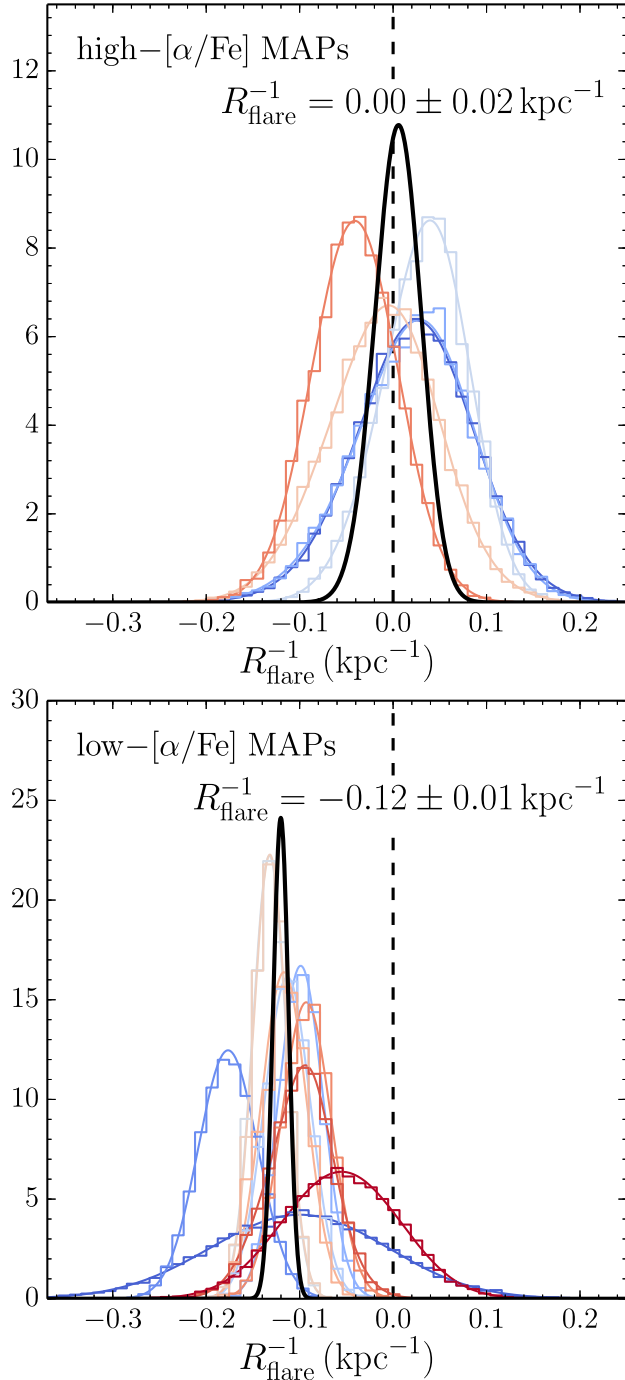


FIG. 12.— Flaring of individual MAP disk components. The PDFs for the inverse flaring scale length R_{flare}^{-1} for individual MAPs for well-populated high- $[\alpha/\text{Fe}]$ (*top panel*) and low- $[\alpha/\text{Fe}]$ (*bottom panel*) MAPs are displayed (histogram), together with smooth fits to these PDFs with a sum of two Gaussians (colored curves). The combined PDF obtained by multiplying the individual smooth PDFs is shown in black; its mean and standard deviation are given in the top right. The displayed MAPs are those of Figure 11, with colors ranging from blue to red for low- to high- $[\text{Fe}/\text{H}]$ MAPs. The dashed vertical line indicates the limit of flaring disks (to its left); the high- $[\alpha/\text{Fe}]$ MAPs display no flaring to high precision, while the low- $[\alpha/\text{Fe}]$ MAPs are consistent with a single flaring scale length of $R_{\text{flare}} \approx 8.5 \pm 0.7$ kpc.

Figures 12, 13, 14, and 15. The vertical profile of individual MAPs is difficult to determine from the APOGEE-RC data, because the sample is dominated by low-

latitude fields that give little leverage for measuring the vertical density drop off. When allowing the inverse scale length of the flare (R_{flare}^{-1}) to be free, there is a large degeneracy between R_{flare}^{-1} and the scale height at the solar circle h_Z . Figure 12 displays PDFs for R_{flare}^{-1} for MAPs along the well-populated high- and low- $[\alpha/\text{Fe}]$ sequences. For these MAPs, R_{flare}^{-1} is relatively well constrained. We see from these PDFs that the high- $[\alpha/\text{Fe}]$ MAPs are all consistent with having a constant $h_Z(R)$, while low- $[\alpha/\text{Fe}]$ MAPs show strong evidence for a flaring $h_Z(R)$. The constraints on R_{flare}^{-1} for both $[\alpha/\text{Fe}]$ groups are tight: $R_{\text{flare}}^{-1} = 0.00 \pm 0.02 \text{ kpc}^{-1}$ for the high- $[\alpha/\text{Fe}]$ MAPs and $R_{\text{flare}}^{-1} = -0.12 \pm 0.01 \text{ kpc}^{-1}$ for the low- $[\alpha/\text{Fe}]$ MAPs. The latter corresponds to a flaring scale length of 8.5 ± 0.7 kpc. We illustrate the flaring (and non-flaring) of the MAPs in Figure 13. To further explore what the radial dependence of h_Z is, we have also fit each MAP with the linear and inverse-linear flaring profiles of equation (8). Figure 13 contains these results: the median of the MCMC samples from these fits are very close to that using the exponential model. The gray band for each MAP displays the range in h_Z spanned by the different models. This gray band is only visible for a few low- $[\alpha/\text{Fe}]$ MAPs and mainly near the edges of the radial range, indicating that the low- $[\alpha/\text{Fe}]$ MAPs have an exponential flaring profile to within their uncertainties. For high- $[\alpha/\text{Fe}]$ MAPs the results from the alternative flaring profiles are almost indistinguishable from those with the exponential model.

To determine the scale heights, h_Z , of all of the MAPs, we then repeat the density fits while fixing R_{flare}^{-1} . Specifically, we set $R_{\text{flare}}^{-1} = 0$ for all of the high- $[\alpha/\text{Fe}]$ MAPs, defined here as those with $R_{\text{peak}} < 5$ kpc (see Figure 10), and $R_{\text{flare}}^{-1} = -0.1 \text{ kpc}^{-1}$ otherwise. The resulting $h_Z([\text{Fe}/\text{H}], [\alpha/\text{Fe}])$ is displayed in Figure 14. In addition to the requirement that each MAP needs to have at least 15 stars, we have further removed MAPs for which the uncertainty in h_Z is larger than 20%; this removes a few MAPs at low $[\text{Fe}/\text{H}]$ (both at high and low $[\alpha/\text{Fe}]$). It is clear from this figure that the dependence of h_Z on $([\text{Fe}/\text{H}], [\alpha/\text{Fe}])$ is very smooth, and similar to that found by Bovy et al. (2012c). In particular, intermediate components with $h_Z \approx 500$ pc are prevalent at the low- $[\text{Fe}/\text{H}]$ end of the low- $[\alpha/\text{Fe}]$ sequence and at the high- $[\text{Fe}/\text{H}]$ end of the high- $[\alpha/\text{Fe}]$ sequence.

In § 4.2 we determined that a vertical profile consisting of the sum of two exponentials does not provide a good fit to the broad abundance subsamples. We repeat this exercise here, fitting a model with two vertical exponentials with a constant scale height. In Figure 15 we compare the scale height of the dominant component with that of the secondary component. We constrain the secondary component to contribute at least 15% of the local column density, to remove the large degeneracies at small amplitudes of the secondary component. We find that whenever the secondary component makes a substantial contribution to the column density, its scale height is the same as that of the dominant component. That is, the vertical profile is consistent with being a single exponential.

6. DISCUSSION

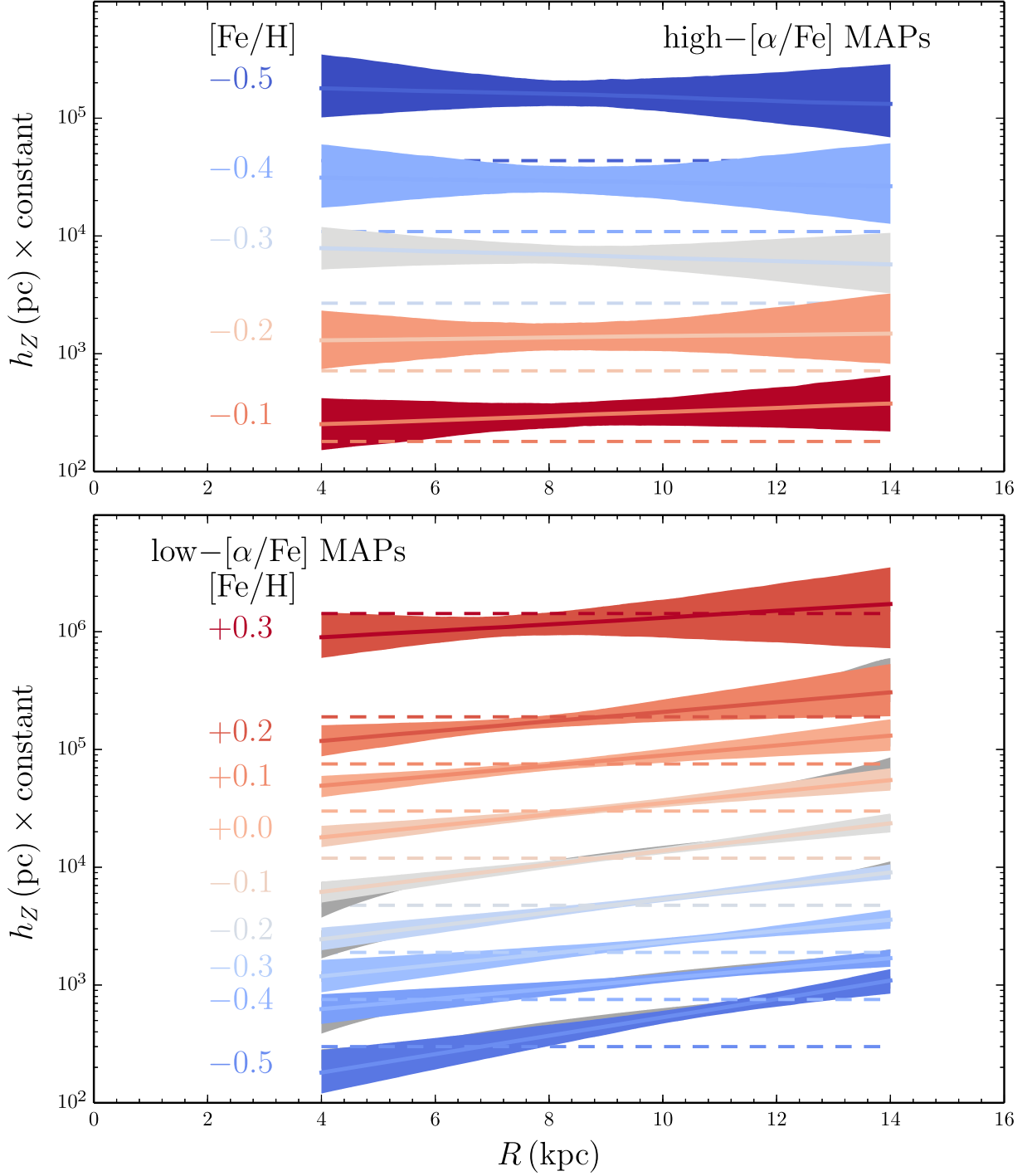


FIG. 13.— Vertical profile of MAPs. This figure displays the radial dependence of the scale height of MAPs along the well-populated high- $[\alpha/\text{Fe}]$ (*top panel*) and low- $[\alpha/\text{Fe}]$ sequence (*bottom panel*; those of Figure 11, except for the lowest- $[\text{Fe}/\text{H}]$ MAP). The colored bands give the 95% uncertainty region around the median displayed as a solid line for the exponential flaring model. The gray band (when visible) shows the range in median profile spanned by all three flaring models (exponential, linear, and inverse-linear; see equations [7] and [8]). A $[\text{Fe}/\text{H}]$ -dependent offset has been applied to the y axis to separate the different MAPs; the dashed horizontal line gives the position of $h_Z = 300$ pc for each MAP. The high- $[\alpha/\text{Fe}]$ MAPs do not flare, while all low- $[\alpha/\text{Fe}]$ MAPs are consistent with an exponential flaring profile with a scale length of $R_{\text{flare}} \approx 8.5 \pm 0.7$ kpc (see Figure 12 above). The scale height increases smoothly from high- to low- $[\text{Fe}/\text{H}]$ MAPs.

This paper is the first to dissect in detail—and over a wide range of Galactocentric radii—the radial structure of the MW’s stellar disk in terms of MAPs, abundance-selected stellar sub-populations. As some of the results of this analysis may appear unorthodox, we first show the

extent to which these results are compatible with earlier analyses, before proceeding to interpret them in a galaxy formation context.

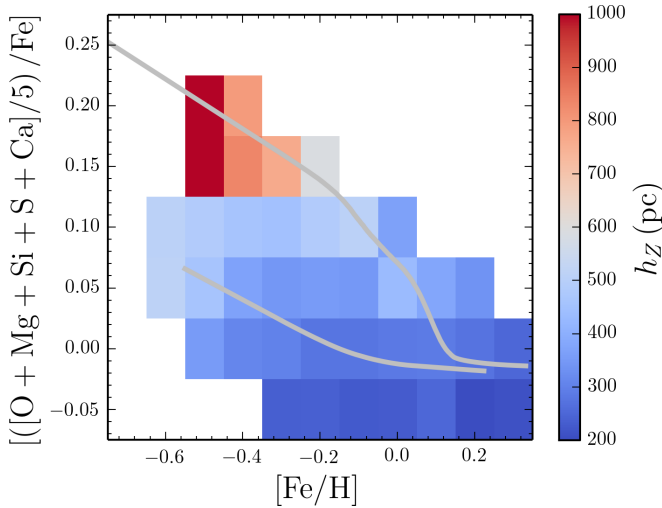


FIG. 14.— Vertical scale height of MAPs. The scale heights, h_Z , for fits assuming a constant scale height with Galactocentric radius for MAPs best fit as a single radial exponential (those labeled “ $R_{\text{peak}} < 5$ kpc” in Figure 10) and for fits with a flaring vertical profile with a flare scale length of 10 kpc for all other MAPs. A few MAPs along the upper and left edges for which the scale height cannot be precisely determined from the present data are omitted. The locus of the high- and low- $[\alpha/\text{Fe}]$ sequences are indicated as in Figure 10. MAPs displays a smooth increase in h_Z as a function of declining $[\text{Fe}/\text{H}]$ and increasing $[\alpha/\text{Fe}]$, even for the conservative flaring model chosen here.

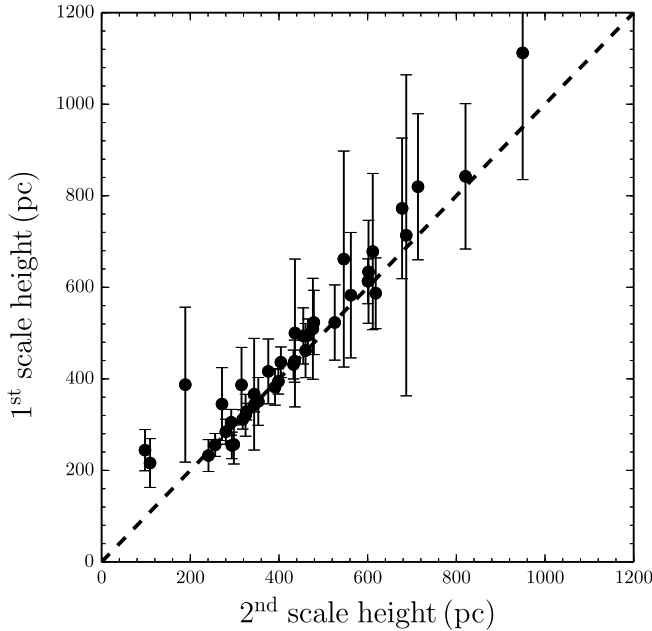


FIG. 15.— Scale height of the dominant component versus that of the secondary component in two-vertical-exponential fits to the MAP spatial densities. The scale heights displayed here are the median of samples from the posterior PDF for which the secondary component provides significantly to the density (defined as contributing more than 15% of the local column density), to avoid the massive degeneracy in the scale height when the amplitude is allowed to be close to zero. The two scale heights are the same for all MAPs, demonstrating that they are well represented as a single vertical exponential. MAPs with very low scale heights, however, show some evidence of a second, even lower scale height.

6.1. Comparison to Bovy et al. (2012c)

For the high- $[\alpha/\text{Fe}]$ MAPs our results on the radial profile are in perfect agreement with those of Bovy et al.

(2012c). They find for a single-exponential fit to $\Sigma(R)$ for high- $[\alpha/\text{Fe}]$ MAPs that $h_R = 2.01 \pm 0.05$ kpc, consistent with our measurement here of $h_R = 2.2 \pm 0.2$ kpc. Their result is more precise because they have $\approx 14,000$ high- $[\alpha/\text{Fe}]$ stars compared to only ≈ 500 here. However, the RC distance scale is more accurately known than that of the G dwarfs used by Bovy et al. (2012c), so larger samples of RC stars should eventually lead to a more accurate and precise measurement of h_R . The improved radial coverage of the APOGEE-RC sample over the G-dwarf sample also allows us to ascertain that $\Sigma(R)$ is indeed a single exponential; this was an assumption in Bovy et al. (2012c).

The present analysis has shown that the radial surface-density profile of low- $[\alpha/\text{Fe}]$ MAPs is *not* a single exponential, but is much better fit as a broken-exponential profile, rising to a peak radius R_{peak} , before falling off. This makes it difficult to meaningfully compare our measurements of $\Sigma(R)$ to measurements in the literature, which typically consist of single-exponential fits to a mix of MAPs.

Bovy et al. (2012c) were the first to dissect the MW disk into narrow abundance bins and while they also fit single-exponential models to $\Sigma(R)$, their results can be more easily compared to the current measurements. For comparison, we have carried out single-exponential fits to the APOGEE data $\Sigma(R)$ (see Table 1), but the different radial coverage makes this a qualitative exercise rather than a quantitative one. On this level, our results are consistent with those of Bovy et al. (2012c) for the low- $[\alpha/\text{Fe}]$ MAPs. When fit with a single-exponential $\Sigma(R)$, low- $[\text{Fe}/\text{H}]$ MAPs have a flat profile, solar- $[\text{Fe}/\text{H}]$ MAPs have a scale length of $h_R = 3.0 \pm 0.1$ kpc, and high- $[\text{Fe}/\text{H}]$ MAPs have $h_R = 1.67 \pm 0.03$ kpc, similar to the results in Figure 5 of Bovy et al. (2012c). It is clear, however, that we significantly refine the results of Bovy et al. (2012c) for the low- $[\alpha/\text{Fe}]$ MAPs here by determining the shape of $\Sigma(R)$.

We find that the vertical profile of the low- $[\alpha/\text{Fe}]$ MAPs consists of a single exponential, but with a scale height that is flaring outward with an approximately exponential profile. Bovy et al. (2012c) assumed a constant $h_Z(R)$, because (unpublished) investigations using the SEGUE G-dwarf data set demonstrated that all but the most extreme flaring models were consistent with the data, and $h_Z(R) = \text{constant}$ was the simplest possible assumption. The inability to determine the flaring of low- $[\alpha/\text{Fe}]$ MAPs by Bovy et al. (2012c) was due to the limited radial coverage (spanning only about ± 2 kpc) and the lack of low latitude lines of sight in SEGUE. We have not attempted to refit the SEGUE G-dwarf data using the best-fit flaring model from this paper, but the slow exponential flaring of $R_{\text{flare}}^{-1} = -0.12 \pm 0.01 \text{ kpc}^{-1}$ is such that it is most likely consistent with the SEGUE G-dwarf data.

The measurements of the scale heights in this paper are much more uncertain than those of Bovy et al. (2012c), because most of the APOGEE lines of sight are concentrated near the plane. Because we do not currently possess the relative calibration of $([\text{Fe}/\text{H}], [\alpha/\text{Fe}])$ in APOGEE and SEGUE we cannot directly compare measurements of h_Z in SEGUE and in APOGEE. However, it is clear that the main trends are the same:

(a) $h_Z([\text{Fe}/\text{H}], [\alpha/\text{Fe}])$ spans the range from 200 pc to 1000 pc, with a smooth transition between these two extremes, (b) the thinnest components have low $[\alpha/\text{Fe}]$ and high $[\text{Fe}/\text{H}]$, (c) the thickest components have high $[\alpha/\text{Fe}]$ and low $[\text{Fe}/\text{H}]$, and (d) intermediate ($h_Z \approx 500$ pc) components lie at the high- $[\text{Fe}/\text{H}]$ end of the high- $[\alpha/\text{Fe}]$ sequence and the low- $[\text{Fe}/\text{H}]$ end of the low- $[\alpha/\text{Fe}]$ sequence. Point (a) here is particularly remarkable, because we measure h_Z much closer to the plane and for isothermal MAPs (Bovy et al. 2012b) in dynamical equilibrium, we expect h_Z to become larger near the plane. We also confirm that each MAP consists of a single vertical exponential component.

6.2. Comparison to star-count measurements

Any quantitative comparison with previous measurements of $\Sigma(R)$ is problematic, because these measurements typically fit single-exponential $\Sigma(R)$, while we find that the radial profile of MAPs is better fit as a broken exponential with a peak radius. We are therefore forced to qualitatively interpret older measurements based on their radial and vertical coverage. The most reliable measurements of the radial structure are based on IR data. Among these, GLIMPSE measurements based on $|b| \leq 1^\circ$ at $10^\circ \leq l \leq 65^\circ$ give $h_R = 3.9 \pm 0.6$ kpc (Benjamin et al. 2005), while COBE near-IR and far-IR disk data at $|b| \leq 30^\circ$ lead to $h_R = 2.3$ kpc (Drimmel & Spergel 2001), and near-IR 2MASS data in the outer disk are best fit with $h_R = 2.2$ kpc (Reyl   et al. 2009). We can explain these differences qualitatively as follows: the GLIMPSE star counts at $|b| \leq 1^\circ$ are dominated by the low- $[\alpha/\text{Fe}]$ MAPs, which in the inner MW are approximately a combination of the “solar” and “high- $[\text{Fe}/\text{H}]$ ” populations in Figure 9 and therefore have quite flat $\Sigma(R)$. The COBE measurements that extend to higher $|b|$ contain a much higher contribution from the short h_R high- $[\alpha/\text{Fe}]$ MAPs, and therefore lead to h_R closer to 2 kpc. The outer-disk 2MASS sample from Reyl   et al. (2009) is dominated by the steep outer scale length of low- $[\alpha/\text{Fe}]$ “solar” populations ($h_R \approx 1.5$ kpc), and the somewhat steep outer profile of “low- $[\text{Fe}/\text{H}]$ ” populations ($h_R \approx 2.7$ kpc; see Table 1); that an overall profile with $h_R = 2.2$ kpc would result appears somewhat likely. While these qualitative comparisons are interesting, they mostly point toward the necessity to perform proper comparisons between the radial profile obtained from different types of tracers and from different parts of the MW disk.

Star counts in the outer disk have found evidence of a break in the stellar surface density (i.e., an abrupt steepening of the already decreasing surface density), with the majority of studies converging on a break around $R \approx 13.5$ kpc (e.g., Reyl   et al. 2009; Sale et al. 2010; Minniti et al. 2011; R. Benjamin et al., 2016, in preparation), with a steep density decline beyond the break ($h_R = 1.2 \pm 0.3$ kpc; Sale et al. 2010). We have found that each MAP has a peak radius, similar in kind to the break radius found in the outer disk, with outer scale lengths $h_{R,\text{out}} \lesssim 2$ kpc (see Figure 11). The break radius seen in star counts using data and methods that do not discern stars by their abundances is therefore most likely nothing more than the outermost of the series of break (or peak) radii displayed by the MAPs; the series in Figure 10 ends around 13 kpc. More metal-poor MAPs fill-in

the density beyond the peak of more metal-rich MAPs until the most metal-poor MAPs are reached, and the total surface-density starts to decline with the steep outer scale length of the most metal-poor low- $[\alpha/\text{Fe}]$ MAPs. Because we simultaneously fit for $\Sigma(R)$ and the flaring of the disk, we can be sure that the steep decline in mid-plane density is truly because of a declining $\Sigma(R)$ and not just a consequence of the flaring of the disk.

6.3. Implications for disk formation and evolution

Our new results on the stellar population dependent structure of the MW disk provide stringent and qualitatively new constraints on models of the formation and evolution of galactic disks. We discuss qualitatively the implications of our results for some of the main evolutionary mechanisms, but more detailed comparisons to models are beyond the scope of this paper.

As displayed in Figures 10 and 11, we find that when the MW disk is dissected into MAPs, it consists of a set of donut-like rings, with a peak radius that is a declining function of $[\text{Fe}/\text{H}]$ for low- $[\alpha/\text{Fe}]$ MAPs. high- $[\alpha/\text{Fe}]$ MAPs have peak radii constrained to be < 5 kpc, and are therefore consistent with a more traditional disk structure. Whether or not they actually display at peak at $0 < R/\text{kpc} < 5$ or are really a single exponential over the full radial range is a question that requires more data at $R < 5$ kpc.

These present-day patterns in the abundance and spatial structure of the disk must be the consequence of the radius-dependent chemical evolution, convolved with the subsequent orbit evolution. One possibility is that what we are seeing at low $[\alpha/\text{Fe}]$ are the (approximate) equilibrium points of chemical evolution, where a steady state of metal consumption and gas dilution is maintained. Most stars in simple chemical-evolution models form near the equilibrium $[\text{Fe}/\text{H}]$, the value of which depends primarily on how much gas is lost to outflows (e.g., Binney & Merrifield 1998; D. Weinberg, et al., 2016, in preparation). Outflows are likely more effective in the outer disk than in the inner disk; this scenario would naturally explain the well-defined radial range spanned by each low- $[\alpha/\text{Fe}]$ MAP and the anti-correlation between $[\text{Fe}/\text{H}]$ and R_{peak} . The radial migration that the low- $[\alpha/\text{Fe}]$ populations have likely experienced (see below) will have smoothed the radial profiles such that the initial radial profile of each low- $[\alpha/\text{Fe}]$ MAP was even more sharply peaked around a single radius.

How do the high- $[\alpha/\text{Fe}]$ MAPs with $R_{\text{peak}} < 5$ kpc fit into this scenario? The radial profiles of MAPs with the same $[\text{Fe}/\text{H}]$ but different $[\alpha/\text{Fe}]$ are strikingly different, especially at low $[\text{Fe}/\text{H}]$. This suggests that they are not connected by an evolutionary track from high- to low- $[\alpha/\text{Fe}]$ at a given $[\text{Fe}/\text{H}]$. The similarity in the radial profile of high- $[\alpha/\text{Fe}]$ MAPs, combined with the narrow range of $[\alpha/\text{Fe}]$ spanned at each $[\text{Fe}/\text{H}]$ along the high- $[\alpha/\text{Fe}]$ sequence (Nidever et al. 2014), points towards formation and evolution scenarios of all high- $[\alpha/\text{Fe}]$ MAPs that were similar enough to be structurally indistinguishable by now. Because high- $[\alpha/\text{Fe}]$ populations are likely to be the oldest populations in the disk (see discussion in Bovy et al. 2012c and Haywood et al. 2013; Bergemann et al. 2014; Martig et al. 2015), this implies that similar physical conditions existed throughout the disk at early times, a conclusion also reached

by Nidever et al. (2014), because of the constant locus of the high- $[\alpha/\text{Fe}]$ sequence in the $([\text{Fe}/\text{H}], [\alpha/\text{Fe}])$ plane throughout the disk. What, if anything, caused this to change for the low- $[\alpha/\text{Fe}]$ sequence remains to be sorted out (e.g., Stinson et al. 2013; Bird et al. 2013).

We have also discovered that the thickness of low- $[\alpha/\text{Fe}]$ MAPs is not constant, but instead flares in an approximately exponential manner (Figures 12 and 13). Such flaring is commonly seen in simulations of the outer disk, because of the dynamical heating due to orbiting satellites and mergers (e.g., Quinn et al. 1993). However, we measure the same level of flaring for the outer-disk, low- $[\text{Fe}/\text{H}]$ MAPs as we do for the centrally-concentrated, high- $[\text{Fe}/\text{H}]$ MAPs. It is improbable that the latter have been affected much by outer-disk satellite heating. Flaring with an exponential profile and at the level that we detect is an important prediction of J_z -conserving radial migration—that is, any redistribution of angular momentum that approximately conserves the vertical action J_z (e.g., Minchev et al. 2012; Solway et al. 2012; Roškar et al. 2013). Therefore, we consider the observed flaring of low- $[\alpha/\text{Fe}]$ MAPs as another important indication that radial migration significantly affects the distribution of low- $[\alpha/\text{Fe}]$ stars. This is in addition to the fact that one needs radial migration to explain the observed lack of correlation between age and metallicity for low- $[\alpha/\text{Fe}]$ stars (e.g., Sellwood & Binney 2002; Schönrich & Binney 2009) and to explain the reversal in the skew of the metallicity distribution function when going from the inner Galaxy to the outer Galaxy (Hayden et al. 2015).

We find at $> 5\sigma$ confidence that the high- $[\alpha/\text{Fe}]$ MAPs do not flare in the same manner as the low- $[\alpha/\text{Fe}]$ MAPs. Instead, we find that they must have nearly constant thicknesses. At face value, this finding implies that little radial migration has occurred in the high- $[\alpha/\text{Fe}]$ populations, because effects such as those from mergers that can undo the flaring by mixing in-situ and migrated populations (Minchev et al. 2014) do not apply to the mono-abundance populations considered here. The fact that large-scale migration does happen for the low- $[\alpha/\text{Fe}]$ populations entails that whatever causes migration likely only strongly affects kinematically-cold populations. Spiral structure whose strength rapidly declines with height is an obvious candidate for such a migration mechanism. However, determining the exact implications of the constant thickness of high- $[\alpha/\text{Fe}]$ populations for the level at which radial migration affects the thicker, high- $[\alpha/\text{Fe}]$ populations requires chemo-dynamical models that employ a realistic model for the diffusion of stellar orbits due to migration-inducing perturbers. Whatever the case may be, the lack of flaring in the high- $[\alpha/\text{Fe}]$ populations makes it unlikely that their thickness is due to migration or satellite heating.

While our measurements of the scale heights of MAPs are noisier than those of Bovy et al. (2012c), they are good enough to confirm the existence and ubiquity of intermediate h_z components and the smoothness of the transition between the traditional “thin” and “thick” disks: the vertical structure of the disk cannot be described by only two structurally distinct components. Overall, the smoothness of the h_z transition, the fact that the high- $[\alpha/\text{Fe}]$, large- h_z MAPs are centrally concentrated, and the level and homogeneity of the flaring

observed in low- $[\alpha/\text{Fe}]$ MAPs all point toward smooth, internal processes dominating the evolution of the MW disk.

Few cosmological simulations exist that can be directly compared to our results. A dissection of the radial profile of galactic disks into mono-abundance or mono-age-metallicity (a convenient proxy for MAPs in simulations) populations has not been attempted in any simulation. The analysis of Stinson et al. (2013) comes closest of any simulation, because they plot the radial profile of MAPs in the MAGIC simulations in their Figure 1 for a few MAPs. However, only a narrow radial range around the solar circle is displayed, and larger-scale trends were not investigated. In agreement with our measurements, they find that high- $[\alpha/\text{Fe}]$ MAPs are well described by single exponentials in the radial direction. For the low- $[\alpha/\text{Fe}]$, low-metallicity MAPs they find flat radial profiles, with some of them showing a shallow peak. However, their low- $[\alpha/\text{Fe}]$, high-metallicity MAPs do not display the broken-exponential that we find here, but are instead consistent with exponentials. Most other recent simulations, such as those of Minchev et al. (2013), Bird et al. (2013), and Martig et al. (2014) only dissect the disk in terms of mono-age populations and find centrally-peaked radial profiles for all such populations. Using $[\alpha/\text{Fe}]$ as an age proxy this does not come as a surprise, as discarding the rich $[\text{Fe}/\text{H}]$ structure in, e.g., Figure 10, will lead to very different radial profiles from those observed for MAPs here. The simplified one-dimensional simulations of a thin, axisymmetric, gravitationally-unstable disk by Forbes et al. (2012) similar to the turbulent disks found in cosmological simulations (e.g., Bournaud et al. 2009) do lead to donut-like mono-age populations by shutting off the gas supply of the inner regions of the disk over time.

The amount of disk flaring for age- or abundance-selected populations in these recent simulations varies, from little to no flaring for undisturbed disks found by Martig et al. (2014) to the strong flaring in the high-resolution simulation studied by Bird et al. (2013). That the high- $[\alpha/\text{Fe}]$ or old populations have a constant thickness while the low- $[\alpha/\text{Fe}]$ or younger populations flare significantly has not been seen in any simulation. If the flaring is due to migration in these simulations, this may indicate that their resolution is not sufficient to distinguish between the response of kinematically cold and warm populations.

The overall thickness of the disk is likely to be constant due to the mix of centrally-concentrated, thick (high- $[\alpha/\text{Fe}]$) components and more extended, thinner-but-flaring (low- $[\alpha/\text{Fe}]$) components. This was also recently found in the simulation of Minchev et al. (2015).

7. CONCLUSIONS

We summarize our main results as follows:

- The excellent radial coverage of APOGEE and its APOGEE-RC subsample has enabled a detailed investigation of the radial structure of abundance-selected components of the disk (MAPs). Any analysis of the spatial density distribution of Galactic low-latitude tracers requires explicit accounting for the 3D dependence of interstellar extinction, even if target selections and observations are in the NIR. We have applied a new likelihood-based formalism (Bovy et al. 2016) for determining the

radial profiles of stellar tracers in the presence of dust extinction. We have been able to obtain good fits to the observed star counts, even in regions of very high extinction, with simple models for the spatial stellar distribution.

- The radial profile of high- $[\alpha/\text{Fe}]$ MAPs is consistent with a single exponential over the large radial range over which they are observed ($4 \lesssim R/\text{kpc} \lesssim 14 \text{ kpc}$), with no sign of a steeper fall-off at large R . Furthermore, all high- $[\alpha/\text{Fe}]$ MAPs are consistent with having *the same* exponential $\Sigma(R)$, with a scale length of $h_R = 2.2 \pm 0.2 \text{ kpc}$. This agrees with the results of Bovy et al. (2012c), who find a common $h_R = 2.01 \pm 0.05 \text{ kpc}$ for the high- $[\alpha/\text{Fe}]$ MAPs and those of Nidever et al. (2014), who find that the high- $[\alpha/\text{Fe}]$ sequence remains in the same place in the $([\text{Fe}/\text{H}], [\alpha/\text{Fe}])$ plane throughout the disk.
- We discovered that the radial surface-density profiles $\Sigma(R)$ of low- $[\alpha/\text{Fe}]$ MAPs are complex: they are not a single exponential and are not even monotonically decreasing outward. Each MAP displays a peak radius R_{peak} with an approximately exponential drop-off away from R_{peak} at smaller and larger radii. Thus, the low- $[\alpha/\text{Fe}]$ stellar disk may be thought of as a sequence of narrow, donut-like annuli of increasing R_{peak} for decreasing $[\text{Fe}/\text{H}]$.
- The peak radius of the low- $[\alpha/\text{Fe}]$ MAPs depends strongly on metallicity, peaking far inside the solar radius for the metal-rich low- $[\alpha/\text{Fe}]$ MAPs, and well outside the solar circle for the metal-poor low- $[\alpha/\text{Fe}]$ MAPs. This is consistent with the known radial metallicity gradient. The MAP with solar abundances peaks at the solar radius, clearly demonstrating that the Sun is typical for its Galactic location.
- The thickness of the high- $[\alpha/\text{Fe}]$ MAPs is constant with R and does not display any flaring. The constraint on the inverse flaring scale length of a model with exponential flaring is strong: $R_{\text{flare}}^{-1} = 0.00 \pm 0.02 \text{ kpc}^{-1}$, when combining constraints from multiple MAPs. This argues against the local vertical structure of the thick disk components being set by outward radial migration.
- Low- $[\alpha/\text{Fe}]$ MAPs present clear evidence of flaring, with an exponential $h_Z(R)$ profile and a common flaring scale length of $8.5 \pm 0.7 \text{ kpc}$. This flaring is present both for low- $[\text{Fe}/\text{H}]$, outer-disk MAPs and for high- $[\text{Fe}/\text{H}]$, inner-disk MAPs.
- We confirm the result of Bovy et al. (2012c), who found that all MAPs have a single vertical scale height, with a continuous distribution of them from the thinnest to the thickest components of the disk. The high precision abundances from APOGEE ($\sigma_{[\text{Fe}/\text{H}]} \approx 0.05 \text{ dex}$ and $\sigma_{[\alpha/\text{Fe}]} \approx 0.02 \text{ dex}$) renders it unlikely that this smooth increase in h_Z is due to contamination between nearby abundance bins.

The measurements of the vertical profile of MAPs here are somewhat noisy, because of a lack of data at intermediate and high latitudes. To make progress on this front requires high-latitude data with a known selection function. Such data will be provided by the APOGEE-2 survey (Sobeck et al. 2014).

We have not attempted to determine updated total stellar surface densities $\Sigma(R_0)$ or total disk masses associated with each MAP here, as was done by Bovy et al. (2012a) for the SEGUE G-dwarf sample. Doing so for the

RC tracers defined using the cuts of Bovy et al. (2014) has large uncertainties, because the manner in which giants trace the underlying population depends on the star formation history. Additionally, the severe cuts used to define the RC make the sampling of the underlying stellar population highly non-trivial. We plan to determine total stellar-population masses for the MAPs in the future by using the full APOGEE giant sample and the SEGUE G-dwarf sample in combination with the spatial densities measured here.

The current results provide greatly improved constraints on the global abundance-spatial distribution of stars, which calls for rigorous and global chemical-evolution modeling. As age constraints for stars beyond the solar neighborhood ($\gtrsim 1 \text{ kpc}$) become available for extensive samples, generalizing the current analysis to include age in addition to abundances in defining MAPs will be an obvious step. This opens up the prospect of a global map of the Galactic disk in age-abundance-position space, even before the release of *Gaia* data.

It is a pleasure to thank the anonymous referee, Brett Andrews, Bob Benjamin, and Chris McKee for helpful comments and discussions. Some of the results in this paper have been derived using the HEALPix (Górski et al. 2005) and *healpy* packages. J.B. received support from a John N. Bahcall Fellowship and the W.M. Keck Foundation. H.W.R. received funding for this research from the European Research Council under the European Union’s Seventh Framework Programme (FP 7) ERC Grant Agreement n. [321035]. T.C.B. acknowledges partial support for this work from grants PHY 08-22648; Physics Frontier Center/Joint Institute or Nuclear Astrophysics (JINA), and PHY 14-30152; Physics Frontier Center/JINA Center for the Evolution of the Elements (JINA-CEE), awarded by the US National Science Foundation. J.B. and H.W.R. acknowledge the generous support and hospitality of the Kavli Institute for Theoretical Physics in Santa Barbara during the ‘Galactic Archaeology and Precision Stellar Astrophysics’ program, where some of this research was performed.

Funding for SDSS-III has been provided by the Alfred P. Sloan Foundation, the Participating Institutions, the National Science Foundation, and the U.S. Department of Energy Office of Science. The SDSS-III web site is <http://www.sdss3.org/>.

SDSS-III is managed by the Astrophysical Research Consortium for the Participating Institutions of the SDSS-III Collaboration including the University of Arizona, the Brazilian Participation Group, Brookhaven National Laboratory, Carnegie Mellon University, University of Florida, the French Participation Group, the German Participation Group, Harvard University, the Instituto de Astrofísica de Canarias, the Michigan State/Notre Dame/JINA Participation Group, Johns Hopkins University, Lawrence Berkeley National Laboratory, Max Planck Institute for Astrophysics, Max Planck Institute for Extraterrestrial Physics, New Mexico State University, New York University, Ohio State University, Pennsylvania State University, University of Portsmouth, Princeton University, the Spanish Participation Group, University of Tokyo, University of Utah, Vanderbilt University, University of Virginia, University of Washington,

REFERENCES

- Abadi, M. G., Navarro, J. F., Steinmetz, M., & Eke, V. R. 2003, *ApJ*, 597, 21
- Adibekyan, V. Z., Sousa, S. G., Santos, N. C., et al. 2012, *A&A*, 545, A32
- Alam, S., Albareti, F. D., Allende Prieto, C., et al. 2015, *ApJS*, 219, 12
- Anders, F., Chiappini, C., Santiago, B. X., et al. 2014, *A&A*, 564, A115
- Audouze, J., Tinsley, B. M. 1976, *ARA&A*, 14, 43
- Bailey, S. 2012, *PASP*, 124, 1015
- Benjamin, R. A., Churchwell, E., Babler, B. L., et al. 2005, *ApJ*, 630, L149
- Bensby, T., Feltzing, S., Lundström, I., & Ilyin, I. 2005, *A&A*, 433, 185
- Bensby, T., Alves-Brito, A., Oey, M. S., Yong, D., & Meléndez, J. 2011, *ApJ*, 735, L46
- Bergemann, M., Ruchti, G. R., Serenelli, A., et al. 2014, *A&A*, 565, A89
- Binney, J. & Merrifield, M. 1998, *Galactic Astronomy* (Princeton, NJ: Princeton Univ. Press)
- Bird, J. C., Kazantzidis, S., Weinberg, D. H., et al. 2013, *ApJ*, 773, 43
- Bournaud, F., Elmegreen, B. G., & Martig, M. 2009, *ApJ*, 707, L1
- Bovy, J., Rix, H.-W., & Hogg, D. W. 2012a, *ApJ*, 751, 131
- Bovy, J., Rix, H.-W., Hogg, D. W., et al. 2012b, *ApJ*, 755, 115
- Bovy, J., Rix, H.-W., Liu, C., et al. 2012c, *ApJ*, 753, 148
- Bovy, J., & Rix, H.-W. 2013, *ApJ*, 779, 115
- Bovy, J., Nidever, D. L., Rix, H.-W., et al. 2014, *ApJ*, 790, 127
- Bovy, J., Rix, H.-W., Green, G. M., et al. 2016, *ApJ*, 818, 130
- Bressan, A., Marigo, P., Girardi, L., et al. 2012, *MNRAS*, 427, 127
- Brook, C. B., Kawata, D., Gibson, B. K., & Freeman, K. C. 2004, *ApJ*, 612, 894
- Carollo, D., Beers, T. C., Chiba, M., et al. 2010, *ApJ*, 712, 692
- Chen, B., Stoughton, C., Smith, J. A., et al. 2001, *ApJ*, 553, 184
- Chen, L., Hou, J. L., & Wang, J. J. 2003, *AJ*, 125, 1397
- Churchwell, E., Babler, B. L., Meade, M. R., et al. 2009, *PASP*, 121, 213
- Dalcanton, J. J., Williams, B. F., Lang, D., et al. 2012, *ApJS*, 200, 18
- Drimmel, R., & Spergel, D. N. 2001, *ApJ*, 556, 181
- Drimmel, R., Cabrera-Lavers, A., & López-Corredoira, M. 2003, *A&A*, 409, 205
- Edvardsson, B., Andersen, J., Gustafsson, B., et al. 1993, *A&A*, 275, 101
- Eisenstein, D., Weinberg, D. H., Agol, E., et al. 2011, *AJ*, 142, 72
- Forbes, J., Krumholz, M., & Burkert, A. 2012, *ApJ*, 754, 48
- Foreman-Mackey, D., Hogg, D. W., Lang, D., & Goodman, J. 2013, *PASP*, 125, 306
- Fuhrmann, K. 1998, *A&A*, 338, 161
- García Pérez, A. E., Allende Prieto, C., Holtzman, J. A., et al. 2015, *AJ*, submitted
- Gilmore, G., & Reid, N. 1983, *MNRAS*, 202, 1025
- Goodman, J. & Weare, J. 2010, *Comm. App. Math. and Comp. Sci.*, 5, 65
- Górski, K. M., Hivon, E., Banday, A. J., et al. 2005, *ApJ*, 622, 759
- Green, G. M., Schlafly, E. F., Finkbeiner, D. P., et al. 2015, *ApJ*, 810, 25
- Gunn, J. E., Siegmund, W. A., Mannery, E. J. et al. 2006, *AJ*, 131, 2332
- Hayden, M. R., Holtzman, J. A., Bovy, J., et al. 2014, *AJ*, 147, 116
- Hayden, M. R., Bovy, J., Holtzman, J. A., et al. 2015, *ApJ*, 808, 132
- Haywood, M., Di Matteo, P., Lehnert, M. D., Katz, D., & Gómez, A. 2013, *A&A*, 560, A109
- Holtzman, J. A., Shetrone, M., Johnson, J. A., et al. 2015, *AJ*, 150, 148
- Jurić, M., Ivezić, Ž., Brooks, A., et al. 2008, *ApJ*, 673, 864
- Kent, S. M., Dame, T. M., & Fazio, G. 1991, *ApJ*, 378, 131
- Laney, C. D., Jone, M. D., & Pietrzyński, G. 2012, *MNRAS*, 419, L1637
- Loebman, S. R., Roškar, R., Debattista, V. P., et al. 2011, *ApJ*, 737, 8
- Majewski, S. R., Zasowski, G., Nidever, D. L. 2011, *ApJ*, 739, 25
- Majewski, S. R., Schiavon, R. P., Frinchaboy, P. M., et al. 2015, *AJ*, submitted
- Marshall, D. J., Robin, A. C., Reylé, C., Schultheis, M., & Picaud, S. 2006, *A&A*, 453, 635
- Martig, M., Minchev, I., & Flynn, C. 2014, *MNRAS*, 442, 2474
- Martig, M., Rix, H.-W., Silva Aguirre, V., et al. 2015, *MNRAS*, 451, 2230
- Mészáros, S., Holtzman, J., García Pérez, A. E., et al. 2013, *AJ*, 146, 133
- Minchev, I. & Famaey, B. 2010, *ApJ*, 722, 112
- Minchev, I., Famaey, B., Quillen, A. C., et al. 2012, *A&A*, 548, A127
- Minchev, I., Chiappini, C., & Martig, M. 2013, *A&A*, 558, A9
- Minchev, I., Chiappini, C., & Martig, M. 2014, *A&A*, 572, A92
- Minchev, I., Martig, M., Streich, D., et al. 2015, *ApJ*, 804, L9
- Minniti, D., Saito, R. K., Alonso-García, J., Lucas, P. W., & Hempel, M. 2011, *ApJ*, 733, L43
- Nidever, D. L., Bovy, J., Bird, J. C., et al. 2014, *ApJ*, 796, 38
- Nidever, D. L., Holtzman, J. A., Allende Prieto, C., et al. 2015, *AJ*, 150, 173
- Nordström, B., Mayor, M., Andersen, J., et al. 2004, *A&A*, 418, 989
- Önehag, A., Gustafsson, B., & Korn, A. 2014, *A&A*, 562, A102
- Prochaska, J. X., Naumov, S. O., Carney, B. W., McWilliam, A., & Wolfe, A. M. 2000, *AJ*, 120, 2513
- Quinn, P. J., Hernquist, L., & Fullagar, D. P. 1993, *ApJ*, 403, 74
- Reddy, B. E., Lambert, D. L., & Allende Prieto, C. 2006, *MNRAS*, 367, 1329
- Reylé, C., Marshall, D. J., Robin, A. C., & Schultheis, M. 2009, *A&A*, 495, 819
- Roškar, R., Debattista, V. P., & Loebman, S. R. 2013, *MNRAS*, 433, 976
- Rix, H.-W. & Bovy, J. 2013, *A&A Rev.*, 21, 61
- Sale, S. E., Drew, J. E., Knigge, C., et al. 2010, *MNRAS*, 402, 713
- Sale, S. E., Drew, J. E., Barentsen, G., et al. 2014, *MNRAS*, 443, 2907
- Schlafly, E. F., & Finkbeiner, D. P. 2011, *ApJ*, 737, 103
- Schönrich, R., & Binney, J. 2009, *MNRAS*, 396, 203
- Sellwood, J. A., & Binney, J. J. 2002, *MNRAS*, 336, 785
- Shetrone, M., Bizyaev, D., Lawler, J. E., et al. 2015, *ApJS*, 221, 24
- Skrutskie, M. F., Cutri, R. M., Stiening, R., et al. 2006, *AJ*, 131, 1163
- Sobeck, J., Majewski, S., Hearty, F., et al. 2014, in *American Astronomical Society Meeting Abstracts*, 223, #440.06
- Solway, M., Sellwood, J. A., & Schönrich, R. 2012, *MNRAS*, 422, 1363
- Stinson, G. S., Bovy, J., Rix, H.-W., et al. 2013, *MNRAS*, 436, 625
- van Dokkum, P. G., Leja, J., Nelson, E. J., et al. 2013, *ApJ*, 771, L35
- Vera-Ciro, C., D’Onghia, E., Navarro, J., & Abadi, M. 2014, *ApJ*, 794, 173
- Vera-Ciro, C. & D’Onghia, E. 2015, *ApJ*, submitted (arXiv:1508.05965)
- Wilson, J. C., Hearty, F., Skrutskie, M. F., et al. 2010, *Proc. SPIE*, 7735, 46
- Wisnioski, E., Förster Schreiber, N. M., Wuyts, S., et al. 2015, *ApJ*, 799, 209
- Wright, E. L., Eisenhardt, P. R. M., Mainzer, A. K., et al. 2010, *AJ*, 140, 1868
- Yanny, B., Rockosi, C., Newberg, H. J., et al. 2009, *AJ*, 137, 4377
- Yoshii, Y. 1982, *PASJ*, 34, 365
- Yuan, H. B., Liu, X. W., & Xiang, M. S. 2013, *MNRAS*, 430, 2188
- Zamora, O., García-Hernández, D. A., Allende Prieto, C., et al. 2015, *AJ*, 149, 181
- Zasowski, G., Johnson, J. A., Frinchaboy, P. M., et al. 2013, *AJ*, 146, 81